High-Modulus Modifications: Stress-Resilient Electrode Materials for Stable Lithium-Ion Batteries

Xiaodi Jiang,[1,§] Mingze Ji,[1,§] Guohua Gao [●],[1,*] Xu Yan,[2] Zheng Xu [●],[2] Wenchao Bi,[3] Qian Cheng [●],[2,†] and Guangming Wu[1,‡]

[1]*Shanghai Key Laboratory of Special Artificial Microstructure Materials and Technology, School of Physics Science and Engineering, Tongji University, Shanghai 200092, China*

[2]*Institute of Acoustics, School of Physics Science and Engineering, Tongji University, Shanghai 200092, China*

[3]*Departments of Physics, College of Science, University of Shanghai for Science and Technology, Shanghai 200093, China*

The stability of lithium-ion batteries is of paramount importance for their commercialization. However, strategies for improving electrode stability are still quite unsatisfactory due to the unclear mechanism of diffusion-induced stress and especially the regulation methods based on it. Herein, based on a columnar lithium-ion diffusion electrode model, a double high-elastic-modulus modification (DHEMM) method is proposed to inhibit deformation and relieve the generated stress during cycling. In this light, TiO_2/V_2O_5/polypyrrole (PPy) nanofibers are accordingly synthesized with a significantly enhanced rate capacity (198.2 mAh g^{-1} at 1600 mA g^{-1}) and electrochemical stability (91.9% capacity retention for 100 cycles at 100 mA g^{-1}), offering an alternative way to fabricate stable lithium-ion batteries.

I. INTRODUCTION

Rechargeable lithium-ion batteries (LIBs) have achieved great success in portable electronics [1]. However, increasing the stability of lithium-ion battery electrodes remains a significant challenge that must be addressed to satisfy practical demands such as hybrid electric vehicles and electrical grids [2,3]. During charge and discharge processes, cracks in lithium-ion electrodes including graphite [4], $LiCoO_2$ [5], $LiMn_2O_4$ [6], and $LiFePO_4$ [7] are commonly encountered, which significantly limits the battery stability. Previous studies have suggested that the mechanical degradation of electrodes caused by cracks mainly results from diffusion-induced stress (DIS) due to inhomogeneous volume change incurred by lithium insertion and desertion [8]. Hence, numerous methods (nanostructuring [9,10], surface modification [11,12], doping [13,14], etc.) have been reported to reduce the volume change and DIS in electrodes to acquire stable LIBs. However, more targeted design strategies based on theoretical predictions to alleviate the DIS in electrodes are still lacking.

Understanding the stress-diffusion behavior and electrochemical attenuation mechanisms is of great interest as it can enable us to develop guidelines for stable electrodes [15,16]. Many studies have focused on building mathematical lithium-ion diffusion models to quantitatively analyze the DIS and volume change of electrodes that occur during lithium-ion diffusion. Prussin first developed a mathematical stress-diffusion model by correlating concentration with temperature to acquire a chemically induced stress distribution in silicon wafers [17]. Following this ansatz, Newman *et al.* developed a two-way coupling model based on chemical and mechanical behaviors to describe stress generation and distribution in spherical electrodes [18]. Furthermore, to better understand and predict DIS, Zhang *et al.* developed a stress-diffusion coupling model that considers both mechanical stress and lithium diffusion in a $LiMn_2O_4$ cathode, and shows that a larger electrode particle results in greater DIS [19]. As research has progressed, an increasing number of factors that influence DIS and volume change have been considered in the electrode diffusion model, such as the electrode particle microstructure [20], surface stress [21], elastic modulus [22], etc., and several studies have highlighted the significance of the elastic modulus in determining the distribution of DIS. Cheng *et al.* showed that the surface modulus can lower the DIS of nanoparticles [23]. By employing a voxel-based finite-element method for stress analysis, Ohashi *et al.* found that stress is concentrated on the material with a

---

*gao@tongji.edu.cn

†q.cheng@tongji.edu.cn

‡wugm@tongji.edu.cn

§Xiaodi Jiang, Mingze Ji contributed equally

high Young's modulus in a composite electrode, which decreases the stress in the electrode [24]. In light of the correlation between the modulus and DIS, researchers have endeavored to design composite components with appropriate elastic modulus to mitigate DIS and the deformation of electrodes. Hao *et al.* developed a mathematical model for a core-shell electrode ($LiMn_2O_4$/C) and showed that DIS of the core is greatly affected by the elastic modulus of the carbon shell, in that it decreases as the shell modulus increases [22]. Furthermore, the active material in a trilayer electrode was proved to have superior mechanical stability during the electrochemical process due to its synergy with the other two protective layers [25–27]. As identified in Si/SiO_2/C, protective SiO_2 and elastic interlayered C can work collaboratively in electrodes to buffer volume changes more effectively [28]. Unfortunately, current studies still revolve around vague associations and lack quantitative analysis when investigating the influence of multiple protective layers on decreasing DIS during lithiation, resulting in a lack of effective stable electrode design strategies.

In this research, we developed a one-dimensional (1D) electrode model to analyze a trilayer structure modified with two layers of inactive materials and subsequently determined the best modification strategy for stress relief is a double high-elastic-modulus modification (DHEMM). By employing a DHEMM, two common electrode additions with high Young's modulus, TiO_2 [29] and conductive polypyrrole (PPy) [30], were introduced as the inner and outer layer on V_2O_5 by electrospinning and *in situ* polymerization, respectively. The resulting nanostructure's high Young's modulus was evaluated using scanning probe acoustic microscopy (SPAM).

After the lithiation process, the TiO_2/V_2O_5/PPy nanofibers (VTs coated by PPy, VTPs) exhibited the least deformation compared to the unmodified V_2O_5 nanofibers (Vs) and the TiO_2/V_2O_5 nanofibers (Vs supported by TiO_2, VTs) with a monolayer modification, as indicated by the statistical results from scanning electron microscopy (SEM) images. Additionally, simulation results showed that the VTPs experienced the lowest levels of radial stress and tangential stress compared to Vs and VTs. Consequently, the VTPs displayed a highly stable structure and electrochemical performance, retaining 91.9% of their initial capacity after 100 cycles. The combination of theoretical and experimental analysis indicates that DHEMM can effectively prevent electrode cracking by decreasing the deformation and DIS, thereby offering an alternative dimension for designing stable LIB electrodes.

II. TRILAYER MODELING

While multilayer electrode design has demonstrated effectiveness in suppressing electrode cracks, there remains a lack of precise theoretical optimization aimed at

significantly enhancing the stability of electrodes. Based on the numerical simulation results from a columnar electrode model, this study proposes a design principle of an electrochemical stable trilayer electrode, which involves the incorporation of two high-modulus protective layers.

The discussed material with a smaller cross-section scale compared with its length can be regarded as a 1D cylindrical object with a long longitudinal axis [Fig. 12 in Appendix A]. Additionally, the cross-section area and its shape do not change along the longitudinal axis. During battery discharge, lithium ions are inserted into the cathode from the electrolyte in the radial direction while the direction of hydrostatic pressure remains unchanged along the longitudinal axis. Since the electrode material is cured on a current collector, it is considered that both ends are under the fixed constraint condition. If the material is regarded as an elastic body that satisfies the generalized plane strain condition, its displacement occurs in the cross section. Using a symmetrical cylindrical coordinate system (r, θ, z), there are three stress components: radial stress σ_r, tangential stress σ_θ, and body stress σ_z. Based on the previous description, we need to consider only two of them, i.e., radial stress σ_r and tangential stress σ_θ, then this case is simplified to a two-dimensional problem.

Based on the equilibrium equation [22],

$$\frac{d\sigma_r}{dr} + \frac{2(\sigma_r - \sigma_\theta)}{r} = 0, \tag{1}$$

constitutive equations of the two stress components in the cylindrical coordinate system are written as

$$\sigma_r = \frac{E}{(1-\nu)(1+\nu)}\left[\varepsilon_r + \nu\varepsilon_\theta - (1+\nu)\frac{\Omega}{3}C\right],$$
$$\sigma_\theta = \frac{E}{(1-\nu)(1+\nu)}\left[\varepsilon_\theta + \nu\varepsilon_r - (1+\nu)\frac{\Omega}{3}C\right], \tag{2}$$

where E is the Young's modulus, ν is the Poisson's ratio, Ω is the partial molar volume, C is the lithium-ion concentration, and radial strain ε_r and tangential strain ε_θ can be written using the small-deformation hypothesis,

$$\varepsilon_r = \frac{du}{dr}, \quad \varepsilon_\theta = \frac{u}{r}. \tag{3}$$

The analytical form of the two stress components can be written as

$$\sigma_r = -\frac{\Omega}{3}E\frac{1}{r^2}\int_{r_0}^{r} Crdr - \frac{E}{1+\nu}\frac{A}{r^2} + \frac{E}{1-\nu}B,$$
$$\sigma_\theta = \frac{\Omega}{3}E\frac{1}{r^2}\int_{r_0}^{r} Crdr - \frac{\Omega}{3}EC + \frac{E}{1+\nu}\frac{A}{r^2} + \frac{E}{1-\nu}B,$$
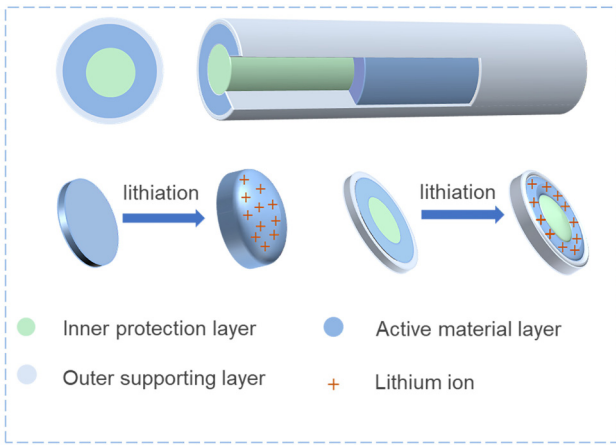$$\tag{4}$$

FIG. 1. Schematic of a trilayer nanofiber structure.

where A and B are two constants. For the concentration of lithium-ion diffusion, due to the constant current condition, the concentration can be calculated from the following [19]:

$$\frac{\partial C}{\partial t} + \nabla \cdot \overrightarrow{J} = 0, \tag{5}$$

where $\overrightarrow{J}$ is the lithium-ion flux. The symbols utilized in our mathematical derivations, as well as detailed information regarding the derivation and related calculations of the numerical solution, are defined and shown in Appendix A. Utilizing this derivation, we developed a 1D model based on equilibrium and diffusion equations to analyze the deformation and DIS of the trilayer structure formed by combining materials. To determine the optimal design strategy, we conducted a comparative stress-strain analysis of the active material with protective layers of varying moduli. As shown in Fig. 1, for a visual representation of the trilayer structure, the configuration containing high Young's modulus materials in both the inner and outer layers is denoted as "HH." Similarly, configurations with low Young's modulus in both inner and outer layers are denoted as "LL," and those with a high (low) Young's modulus inner layer and a low (high) Young's modulus outer layer are labeled as "HL" ("LH").

All parameters used in this simulation are detailed in Tables I and II.

The concentration, DIS, and deformation distribution of the four configurations were calculated using this 1D electrode diffusion model. The number of ions inside the material was guaranteed to be exactly the same for different configurations [Fig. 2(a)]. Among all configurations, HH shows the lowest deformation [Fig. 2(b)], relatively low radial stress distribution [Figs. 2(c) and 2(e)], and lowest tangential stress [Figs. 2(d) and 2(f)] along the radius. Therefore, a DHEMM is proposed to alleviate electrode deformation and DIS during cycling.

III. SYNTHESIS AND CHARACTERIZATION

To validate the effectiveness of the DHEMM method, VTPs were synthesized. V_2O_5 was selected as the electrode active material while TiO_2 and PPy were chosen as the high-modulus modification materials on the inner and outer layer, respectively. For comparison, the Vs and VTs were also synthesized and tested, as described in the following sections. The fabrication process of Vs and VTs involved electrospinning [Fig. S1 in the Supplemental Material [31]] and sintering. To obtain VTPs, we used vacuum chemical vapor deposition for *in situ* polymerization of PPy on VTs.

A. Sample preparation
1. Synthesis of the TiO_2 *sol*

Tetrabutyl titanate, acetic acid, and acetylacetone were dissolved in ethanol as the mixture was stirred magnetically. While stirring, ethanol and deionized water were added dropwise to form a uniform TiO_2 sol.

2. Precursor of Vs and VTs

To prepare Vs, 12 wt % poly(-vinylpyrrolidone) [PVP, weight-average molecular weight (Mw) $\sim 1\,300\,000$] and 8 wt % vanadium(IV)-oxy acetylacetonate [VO(acac)$_2$] were dissolved in dimethyl formamide. The mixture was magnetically stirred at 60 °C for 12 h, yielding a homogeneous green solution.

To prepare VTs, 12 wt % PVP (Mw $\sim 1\,300\,000$) and 9.2 wt % VO(acac)$_2$ were dissolved in dimethyl formamide. The mixture was magnetically stirred at 60 °C for 12 h and yielded a homogeneous green solution. After 3 ml of TiO_2 sol was added, the mixture was magnetically stirred for 3 h to disperse the TiO_2 sol in the solution, yielding a homogeneous green-yellow solution.

3. Fabrication of Vs, VTs, and VTPs

The precursor solution was loaded into a 10-ml syringe for electrospinning, and the system was set up using a 23 gauge stainless needle. The high voltage and distance between the aluminum foil collector and needle were approximately 12 kV and 19 cm, respectively. The flow rate was set to 1 ml/h. In the high electric field, the as-spun

TABLE I. Properties of the trilayer diffusion model.

| Configuration | Young's modulus (Pa) | | |
	Inner material	Middle material	Outer material
HH	10^9	10^7	10^9
HL	10^9	10^7	10^6
LH	10^6	10^7	10^9
LL	10^6	10^7	10^6

TABLE II.   Properties of materials.

Parameters (units)	Inner material	Middle material	Outer material
Poisson's ratio ν	0.30 [22]	0.30 [22]	0.30 [22]
Partial molar volumes Ω (m^3 mol^{-1})	0	3.497×10^{-6} [22]	0
Diffusion coefficient D (cm^2 S^{-1})	0	2.20×10^{-13} [32]	2.18×10^{-12} [32]
Thickness R (m)	0.35×10^{-7}	0.65×10^{-7}	0.84×10^{-8}

Vs and VTs were collected on the aluminum foil. Heating both types of nanofibers (NFs) in air at a rate of 1 °C min^{-1} to 400 °C and maintaining the temperature for 2 h caused the as-spun NFs to oxidize into Vs and VTs. Furthermore, chemical vapor deposition was used to coat a layer of PPy on VTs to form VTPs. VTs were treated with hydrochloric
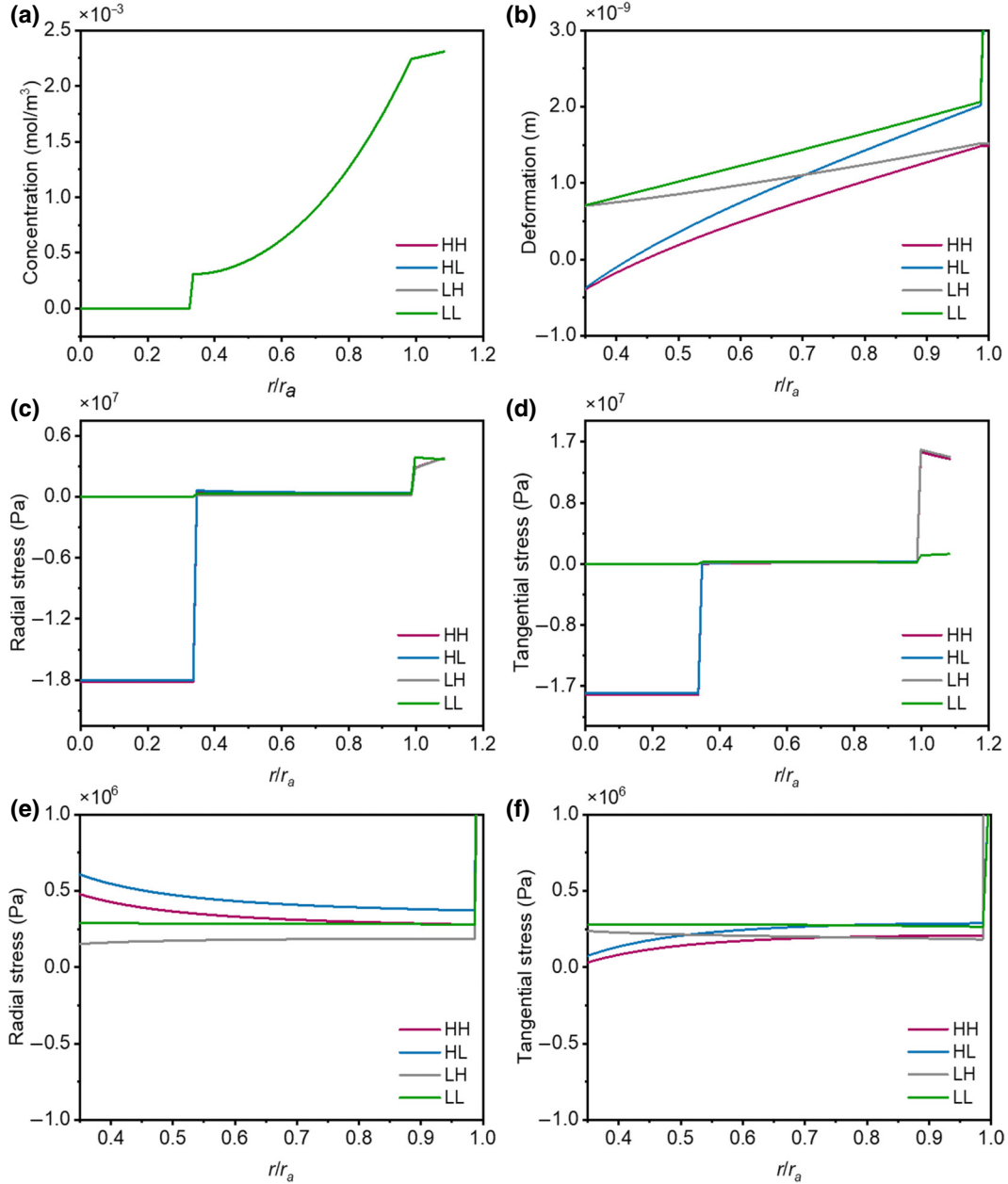

FIG. 2.   Distributions of (a) ion concentration, (b) deformation, (c) radial, and (d) tangential stress in all four configurations of trilayer structure, and (e) radial and (f) tangential stress of active material in the middle layer. r_a is the radius of the interface between middle material and outer material.
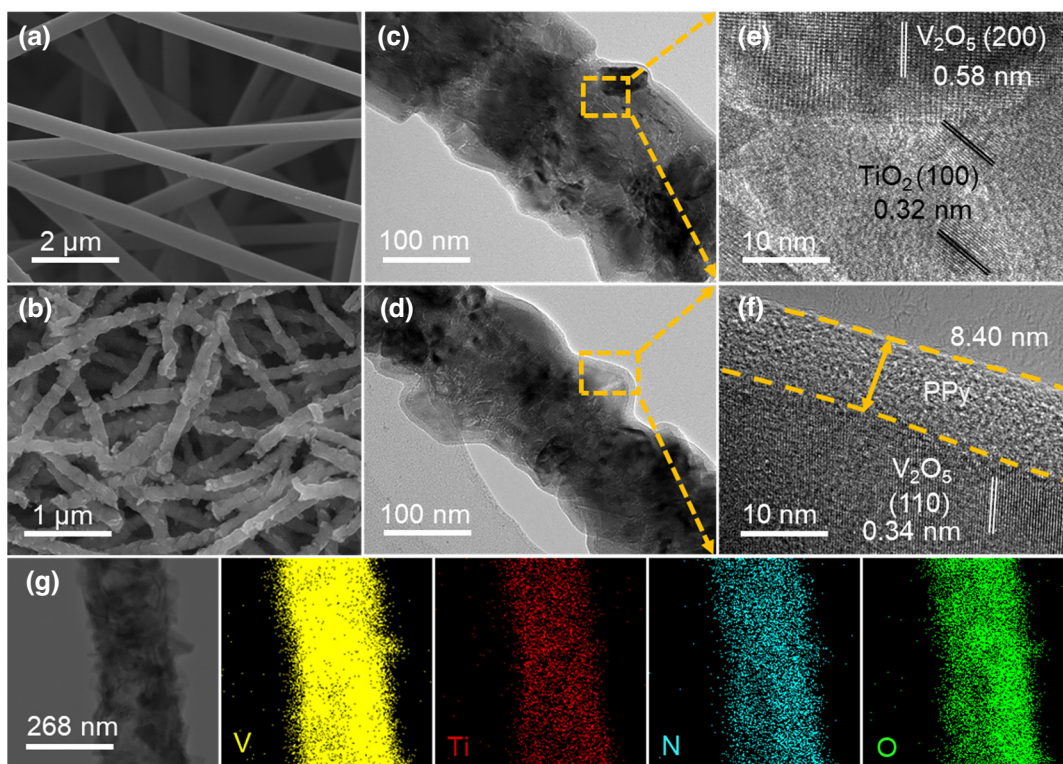
FIG. 3.   SEM images of (a) as-spun VTPs and (b) sintered VTPs. (c),(d) TEM images and (e),(f) corresponding HRTEM images of VTPs. (g) STEM and STEM EDS elemental mapping of the VTPs, and relative intensities of vanadium, titanium, nitrogen, oxygen.

acid vapor (HCl, 0.5 ml 36 wt %) under vacuum at room temperature for 1 h to facilitate PPy oxidative polymerization at the surface of the NFs. Then, 1 ml of pyrrole was polymerized in vacuum conditions at room temperature for 1 h to obtain uniform VTPs.

B. Material characterization

The morphological features of the prepared NFs were studied using field-emission scanning electron microscopy (Philips-XL-30FEG) and transmission electron microscopy (TEM, JEOL-1230). Thermogravimetric and differential scanning calorimetry (TG DSC) measurements were carried out using an SDT Q600 with a heating rate of 10 °C min^{-1} in flowing air. Fourier-transform infrared (FTIR) spectroscopy was performed using a Bruker TENSOR27 within a range from 400 to 4000 cm^{-1}. X-ray photoelectron spectroscopy (XPS) measurements were carried out in a PHI-5300 ESCA1610 SAM instrument equipped with a Mg $K\alpha$ x-ray excitation source (1253.6 eV) at 10 kV and 10 mA. The crystal phase structure was examined by x-ray diffraction (XRD) using a RigakuD/Max-C diffractometer with Cu $K\alpha$ radiation ($\lambda = 1.5406$ Å) between 5° and 60°.

The elasticity modulus was determined using the SPAM technique. SPAM was performed using the Veeco DI 3100

(Veeco, Santa Barbara, CA, USA) system modified with acoustic vibrations, which was developed by the Institute of Acoustics, Tongji University [33,34]. A probe with a tip (silicon) radius of 10 nm and an elastic constant of 0.07791 N/m was used for imaging in contact mode with the scanning rate of 1.03 Hz. The equipment has a precision such that the difference between actual and measured values does not exceed 5% and an accuracy such that the systematic error is less than 0.01% after calibration [35].

C. Electrochemical characterization

The working electrodes were prepared by blending the samples (Vs, VTs, and VTPs) with a carbon back as a conducting agent and polyvinylidene difluoride as a binder at a weight ratio of 7:2:1 in N-methylpyridine solvent, which were uniformly pasted on aluminum foil after stirring for 12 h. After drying under vacuum at 120 °C for 8 h, the electrodes were cut into disks with a diameter of 12 mm with a loading of 0.38 ± 0.06 mg/cm^2. The cells were assembled in an argon-filled glove box with water and oxygen content less than 1 ppm. The configurations of the assembled cells included vanadium oxide materials, Li and a liquid electrolyte [1M LiPF$_6$ in ethylene carbonate and dimethyl carbonate (volume ratio 1:1)]. A polypropylene membrane
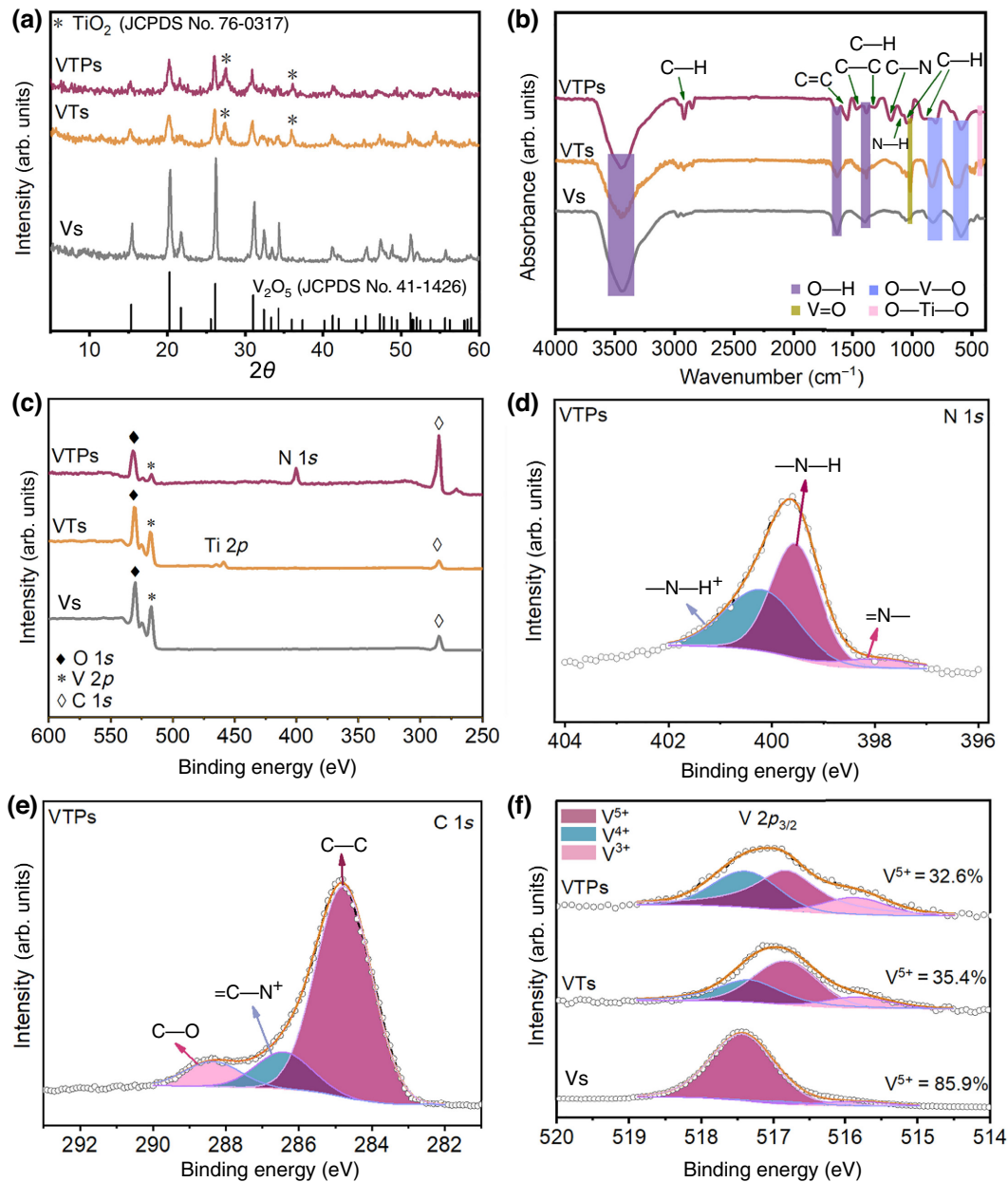
FIG. 4.　(a) XRD patterns and (b) FTIR spectra, (c) full survey XPS spectra of VTPs, VTs and Vs. High-resolution XPS spectra of (d) N 1*s* and (e) C 1*s* of VTPs. (f) High-resolution XPS spectra of V 2*p*$_{3/2}$ of Vs, VTs, and VTPs.

(Celgard 2500) was used as a separator, and lithium metal was used as the counter electrode. Then, the cells were aged for 24 h before electrochemical measurements were taken. The test instruments for electrochemical experiments were a LAND cell-testing system and CHI660C (Chenghua, Shanghai) electrochemical workstation. Electrochemical impedance spectroscopy (EIS) measurements were performed at frequencies from 0.01 Hz to 100 kHz. The high-rate performance was investigated at current densities of 100, 200, 400, 800, and 1600 mA g^{-1}. These tests were performed at room temperature, and the specific

capacity was calculated based on the mass of active materials.

IV. RESULTS AND DISCUSSION

A. Experiments

Figure 3 provides the structural details of VTPs using SEM, TEM, and high-resolution TEM (HRTEM). Figure 3(a) displays the morphology of as-spun VTPs, which exhibits relatively smooth surfaces similar to the as-spun Vs [Fig. 15(a) in Appendix B] and as-spun VTs [Fig. 15(b)
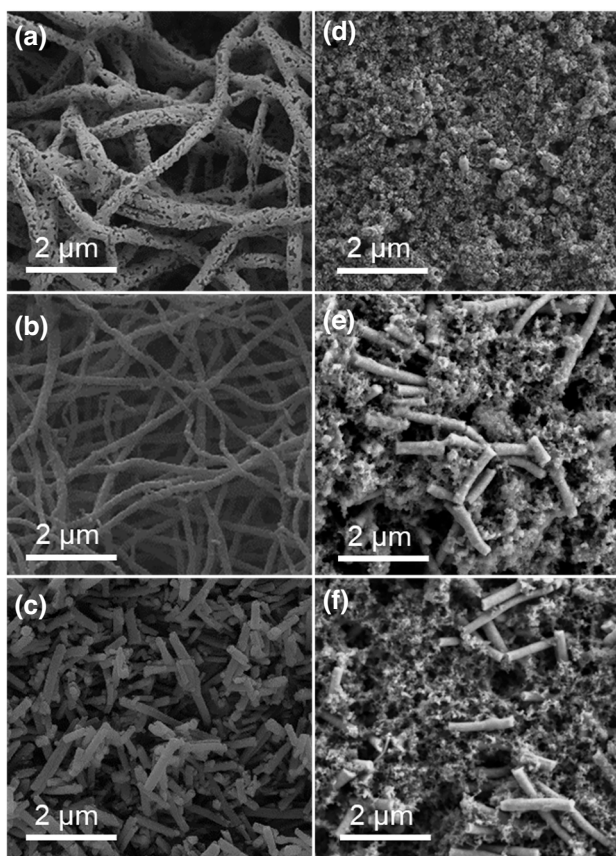
FIG. 5. SEM images before lithiation of (a) Vs, (b) VTs, (c) VTPs and after lithiation of (d) Vs, (e) VTs, (f) VTPs.

in Appendix B]. However, after sintering at 400 °C (1 °C min^{-1}) for 2 h, the morphologies of all samples change from smooth to rough [Figs. 3(b), 15(c), and 15(d) in Appendix B].

This rough morphology arises from the large mass loss that occurs during the sintering process, which can be proved by the TG DSC curve with a peak at 307.2 °C for Vs and 294.2 °C for VTs [Fig. 16 in Appendix B]. This mass loss can be attributed to the decomposition of $VO(acac)_2$ and the degradation of PVP. The second mass loss accompanied by a peak at 430.2 °C for Vs and 440.6 °C for VTs is caused by the crystallization of V_2O_5 [36]. The endothermic peak appearing at 668.7 °C and 674.7 °C may result from the melting of V_2O_5 crystals [37].

During the sintering process, the V_2O_5 and TiO_2 nanoparticles grow gradually and form 1D nanowires [Fig. 3(c)]. Clear lattice fringes with spacings of 0.58 and 0.34 nm can be observed [Figs. 3(e) and 3(f)], corresponding to the (200) and (110) planes of the orthorhombic V_2O_5 phase.

The heterogenous structure of V_2O_5 and TiO_2 are demonstrated in Fig. 3(e). The well-defined lattice fringes with spacing of 0.32 nm are accurately indexed to the (100)

plane of the tetragonal TiO_2 phase. Similar results can also be seen in TEM and HRTEM images of Vs and VTs [Figs. 15(e)–15(h) in Appendix B]. As a protective layer, PPy grows on the outer side of VTs [Fig. 3(d)]. It displays a uniform coating layer on the VTs matrix with a thickness of approximately 8.40 nm [Fig. 3(f)], which is further supported by energy-dispersive x-ray spectroscopy elemental mappings of the high-angle annular dark-field scanning transmission electron microscopy (STEM) [Fig. 3(g)]. Successful preparation of VTPs is indicated by the uniform concentration of the Ti and V elements in the inner layer, as well as the distribution of the N element in the outer layer. Figs. S2–S4 in the Supplemental Material [31] show the SEM images of Vs, VTs, and VTPs before lithiation. The corresponding statistics of fiber diameters for Vs (243.75 ± 5.08 nm), VTs (172.01 ± 3.30 nm), and VTPs (188.83 ± 3.03 nm) are shown in Tables SI–SIII in the Supplemental Material [31]. The difference in the mean values of VT and VTP diameters is almost twice the thickness of the PPy coating observed in Fig. 3(f), which proves the correctness of statistical processes.

XRD patterns were used to determine the crystallinity of Vs, VTs, and VTPs. All diffraction peaks [Fig. 4(a)] of Vs are in accordance with the orthorhombic V_2O_5 phase [Joint Committee on Powder Diffraction Standards (JCPDS) No. 41-1426]. In addition to the characteristic peaks corresponding to V_2O_5, there are extra diffraction angles at 27.4° and 36.0° in the XRD patterns of VTs and VTPs, corresponding to the TiO_2 phase (JCPDS No. 76-0317). The FTIR spectra of Vs, VTs, and VTPs are examined in Fig. 4(b). In the spectrum of Vs, there are two major bands at 586 and 819 cm^{-1}, which are attributed to symmetric and asymmetric stretching modes (ν_s and ν_{as}) of V—O—V, respectively [38,39]. The peak at 1042 cm^{-1} is attributed to the stretching vibration of the terminal V = O bond [39]. The peaks at 914, 1045, 1329, and 2916 cm^{-1} are ascribed to the C—H deformation vibrations and C—H stretching [40,41]. In the spectrum of VTPs, the C—C bond (1472 cm^{-1}) and C = C bond (1551 cm^{-1}) in the pyrrole ring are observed, suggesting the formation of PPy [41]. Absorption bands at approximately 1381, 1626, and 3433 cm^{-1} are caused by O—H bonds from absorbed water [42,43]. In the spectrum of VTs and VTPs, the peak at 436 cm^{-1} is ascribed to the O—Ti—O bond, corresponding to the characteristic peak of TiO_2 [44].

Figure 4(c) shows the full survey XPS spectra of VTPs, VTs, and Vs. The Ti 2p peak (464.1 eV) in Fig. 4(c) from TiO_2 is detected in VTs [45]. Compared with VTs and Vs, a N 1s peak is detected in VTPs, which is the characteristic peak of PPy. The N 1s spectrum [Fig. 4(d)] can be deconvoluted into three peaks centered at 397.8, 399.6, and 400.2 eV, corresponding to =N—, —N—H, and —N—H^+ bonds, respectively [46]. The C 1s spectrum of VTPs [Fig. 4(e)] can be deconvoluted into three peaks corresponding to the C—C (284.8 eV) and C = O
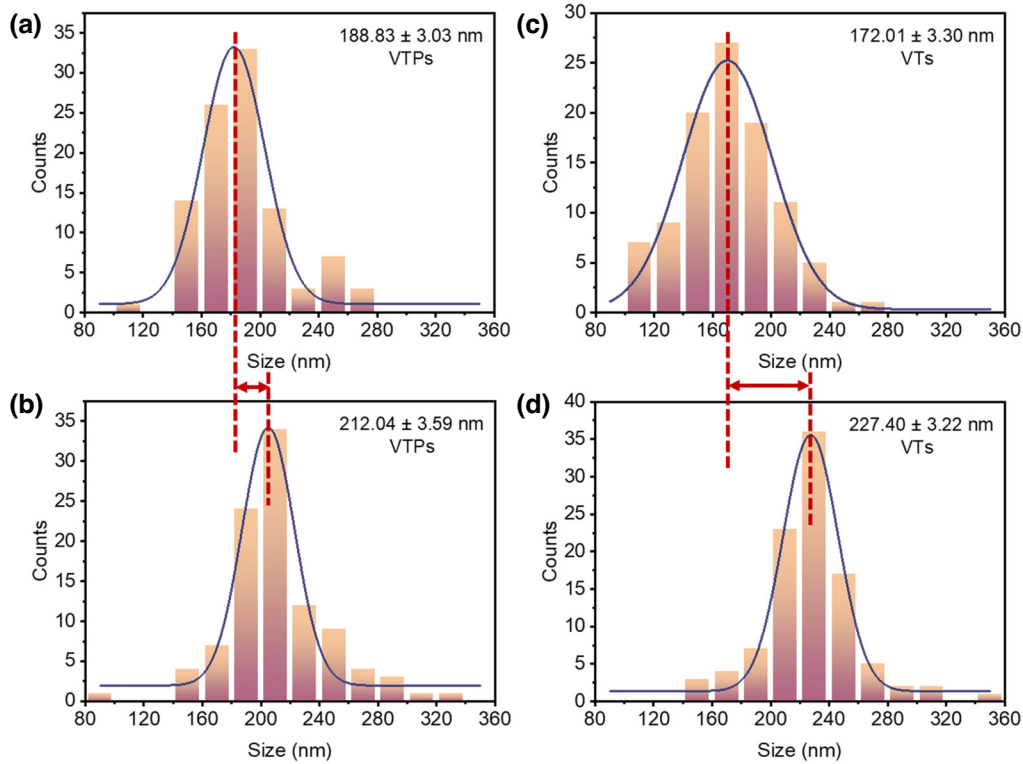
FIG. 6.   Frequency distribution histograms of VTP diameter (a) before and (b) after lithiation, VT diameter (c) before and (d) after lithiation.

(288.4 eV) bonds and the $=C\!\!-\!\!N^+$ (286.5 eV) group in PPy [46]. Figure 4(f) displays the V $2p_{3/2}$ spectra of three samples [12]. The V^{5+} ratio in various valence states (V^{3+}, V^{4+}, and V^{5+}) of VTPs (32.6%) is lower than that in VTs (35.4%) and Vs (85.9%), suggesting that a certain amount of V^{5+} species is reduced to V^{4+} when PPy and TiO_2 are introduced to the surface and interior of V_2O_5. All of these findings suggest the presence of TiO_2 and PPy in VTPs.

Figure 5 shows the morphological changes of Vs, VTs, and VTPs after lithiation. Figures 5(a)–5(c) depict the nanostructure of the three samples before lithiation. As shown in Fig. 5(d), the fiber morphology of Vs disappears after lithiation due to the significant volume change that can easily lead to structure breakage [47]. In contrast, the fiber structural integrity of VTs and VTPs [Figs. 5(e) and 5(f)] is well preserved after lithiation, demonstrating the effectiveness of high-modulus protective layers. As shown in Tables SIV and SV in the Supplemental Material [31], by measuring the diameter of 100 fibers before and after lithiation [Figs. S5–S7 in the Supplemental Material [31]], the diameter change after lithiation for VTPs is significantly smaller than that for VTs [Fig. 6]. The diameters of VTPs and VTs are 212.04 ± 3.59 and 227.40 ± 3.22 nm, respectively, after lithium-ion insertion. The corresponding box plots are also provided [Fig. S8 in the Supplemental Material [31]]. As a result, there is a significantly lower

volume expansion (26.09%) for VTPs compared to VTs (74.77%). This finding implies that the DHEMM strategy is a more effective approach than a single modification in inhibiting volume expansion, ultimately preventing electrode breakage.

B. Numerical simulations

In order to prove the correctness of our theory, we used a 1D model based on the equilibrium and diffusion equations previously mentioned to obtain the distribution of DIS and deformation of Vs, VTs, and VTPs after lithiation [Fig. 7].

The elastic modulus of the electrode is a decisive parameter in DIS distribution through the lithium-ion diffusion model. To achieve high-resolution imaging and study the
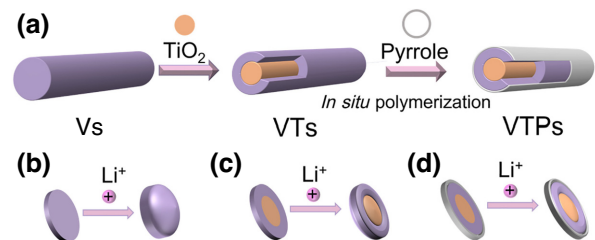

FIG. 7.   (a) Schematic of the structure of Vs, VTs, and VTPs, and schematic of deformation in (b) Vs, (c) VTs, and (d) VTPs after lithiation.
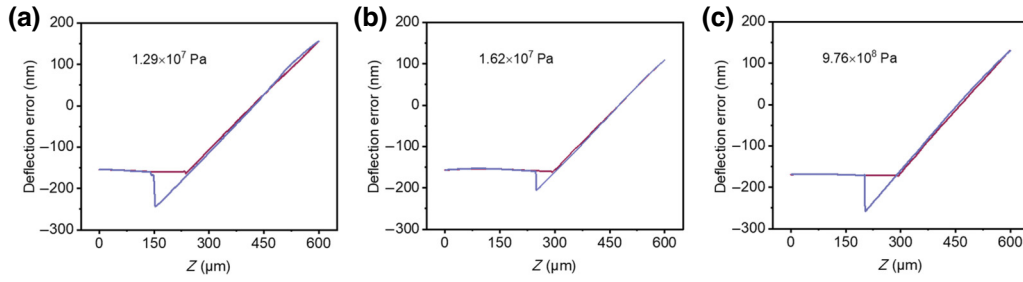
FIG. 8. Force curves of (a) Vs, (b) VTs, and (c) VTPs measured by SPAM.

mechanical properties of micro regions in a nondestructive manner, a SPAM image system was constructed by applying acoustic vibration to the probes of a scanning probe microscope (DI3100) [Fig. S9 in the Supplemental Material [31]]. Figures 17(a)–17(c) in Appendix B show the fibrous characteristics of Vs, VTs, and VTPs via atomic force microscopy (AFM).

Figures 17(d)–17(f) in Appendix B show the SPAM deflection error images (DEIs) of the three samples. DEI measurements are imaged using the difference between the detection signal and the deflection setting values, which can reflect the changes in surface height and are especially sensitive to height mutations. Thus, more high-resolution information related to the subsurface and surface can be observed. Moreover, unlike other surface testing equipment, SPAM phase images can directly show the elastic distributions, which can reveal the spatial distribution of the modulus [Figs. 17(g)–17(i) in Appendix B]. The surface image of VTPs is brighter than those of Vs and VTs, indicating that the VTPs have a higher elastic modulus [Fig. 17(i) in Appendix B].

The initial force curves of three samples [Figs. 8(a)–8(c)] obtained by SPAM were formed by controlling the movement of the probe through the scanning tube and they reveal information on the elasticity of the samples. The abscissa recorded the displacement of the probe over one period of motion, while the ordinate recorded the deflection distance of the cantilever beam. On the basis of force-distance curves, the Hertz model was used to calculate and analyze the contact effect between the probe and the sample under static force to elicit the equation of equivalent elastic modulus $E*$, static force F_0, tip radius R, and indentation depth δ. These four quantities are related as follows [35]:

$$F_0 = -\frac{4}{3}E^*\sqrt{R\delta^3},\tag{6}$$

in which

$$\frac{1}{E^*} = \left(\frac{1-\nu_1^2}{E_1} + \frac{1-\nu_2^2}{E_2}\right).\tag{7}$$

The radius of tip curvature R is set to 10^{-8} m, ν_1 (Poisson's ratio of the tested material) is listed in Table III, ν_2 (Poisson's ratio of the tip) is set to 0.28, and E_1 (the modulus of the tip) is set to 1.70×10^{11} Pa. The initial force curve is the relation of the deflection error (d) and cantilever deflection (Z). Through coordinate transformation, F_0 and δ can be acquired via mathematical relations

$$\delta = Z - d,\tag{8}$$
$$F_0 = kd,\tag{9}$$

where k is set to 0.07791 N/m. Based on these relations, the force-distance curve data were processed in MATLAB to acquire the elastic modulus of the sample.

The moduli obtained by measuring Vs, VTs, and VTPs are 1.29×10^7, 1.62×10^7, and 9.76×10^8 Pa, respectively [Figs. 8(a)–8(c)]. As the SPAM is the characteristic test for surface properties, the moduli of V_2O_5 and PPy layer can be obtained as 1.29×10^7 and 9.76×10^8 Pa, respectively. For more precise calculation, the modulus of TiO_2, which is in the interior of VTs and VTPs, was approximated to the referenced data (2.30×10^{11} Pa) [29].

Meanwhile, the molar ratio V:Ti = 5:1 [Table IV in Appendix B] was measured via energy dispersive x-ray

TABLE III. Properties of materials.

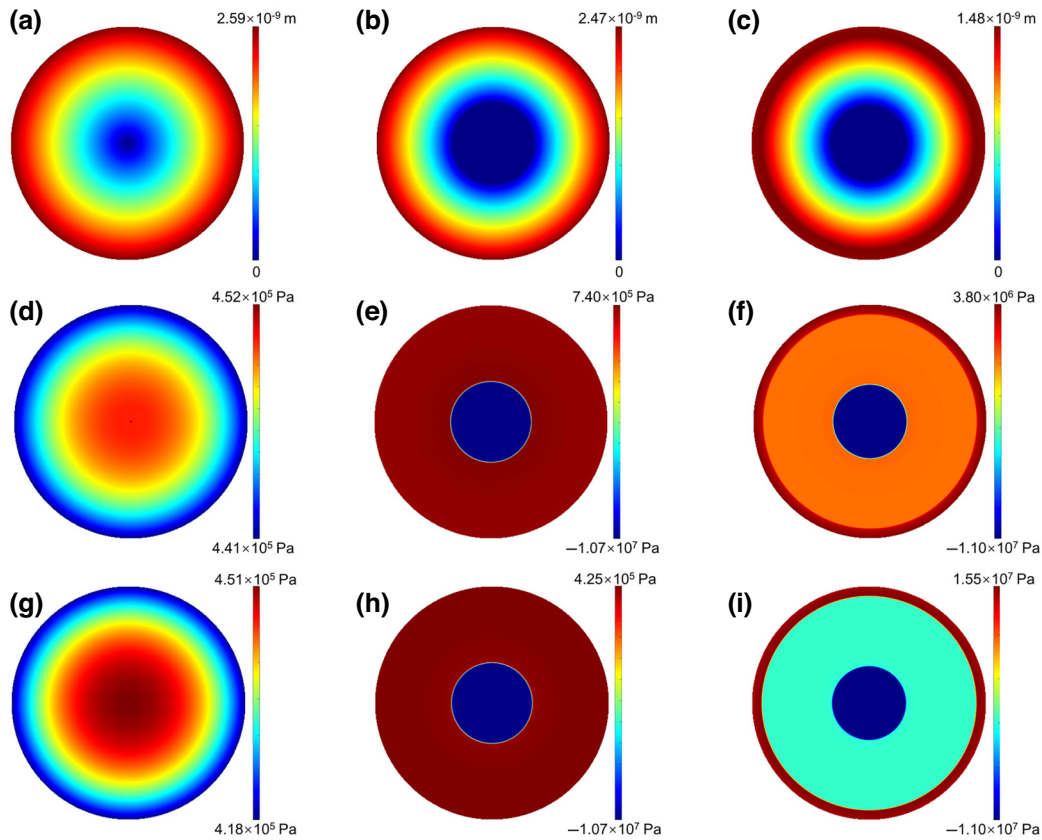| Parameters (units)	TiO_2	V_2O_5	PPy
Young's modulus (Pa)	2.30×10^{11} [29]	1.29×10^7	9.76×10^8
Poisson's ratio ν	0.28 [48]	0.30 [49]	0.43 [50]
Partial molar volumes Ω (m^3 mol^{-1})	0	3.497×10^{-6} [22]	0
Diffusion coefficient D (cm^2 S^{-1})	0	2.20×10^{-13} [32]	2.18×10^{-12} [32]
Thickness R (m)	0.35×10^{-7}	0.65×10^{-7}	0.84×10^{-8}

FIG. 9. Radial distributions of deformation in (a) Vs, (b) VTs, and (c) VTPs, radial stress of (d) Vs, (e) VTs, and (f) VTPs, tangential stress of (g) Vs, (h) VTs, and (i) VTPs.

spectroscopy. Therefore, the radius of the TiO_2 layer is about 35 nm considering the cell volume. The thickness of the V_2O_5 layer is about 65 nm. The material properties of V_2O_5, TiO_2, and PPy are listed in Table III.

During the simulation of Vs, VTs, and VTPs, we kept the overall numbers of ions embedded in the materials consistent for all three structures, as described previously. The lithium-ion concentration in Vs, VTs, and VTPs decreased progressively from the outside to the inside of the NFs [Fig. 18(a) in Appendix B], which is consistent with the law of ion diffusion. Additionally, the difference between each ring element in stress is caused by the gradient distribution of the lithium-ion concentration.

Stress gradually accumulates pointing to the center of the fiber and eventually causes the material to break, which is the main reason for electrode failure. For VTs, to obtain the same number of lithium ions inside the material, more diffusion time is required than for Vs since the TiO_2 inside the material does not participate in lithium-ion transport. For VTPs, the diffusion time is approximately the same but slightly smaller than that for VTs because PPy has a larger diffusion coefficient. Owing to its excellent conductivity, the presence of the outer conductive polymer has no negative effect on ion transmission. In fact, the overall lithium-ion concentration in each ring element in

the material is pulled down in this case because of the extra coating under the same discharge capacity, which leads to a significantly smaller deformation than for the other two.

After a certain amount of ion embedding [Fig. 18(a) in Appendix B], the VTPs exhibit minimal overall deformation, while the overall deformation of Vs is significantly greater than that of the other two [Figs. 9(a)–9(c), and 18(b) in Appendix B]. The radial and tangential stresses are shown in Figs. 18(c)–18(f) in Appendix B, with the corresponding sectional distributions illustrated in Figs. 9(d)–9(i), respectively. As shown in Figs. 18(c) and 18(e) in Appendix B, the radial stress in the TiO_2 layer is smaller than zero, which means it is compressive stress, while that in the V_2O_5 layer is tensile stress. This result shows that the inner support material can effectively suppress the tendency of the V_2O_5 layer to expand towards the center. Meanwhile, in the presence of TiO_2, the tangential stress of the V_2O_5 layer is much smaller because the center takes most of the stress [Figs. 9(g)–9(i), 18(d), and 18(f) in Appendix B]. The higher Young's modulus of TiO_2 compared to V_2O_5 allows it to withstand greater stress without breaking. This concentration of pressure on the protective layer with a higher modulus, rather than on the active material, contributes to the increased mechanical strength of the electrode. However, as a free boundary,
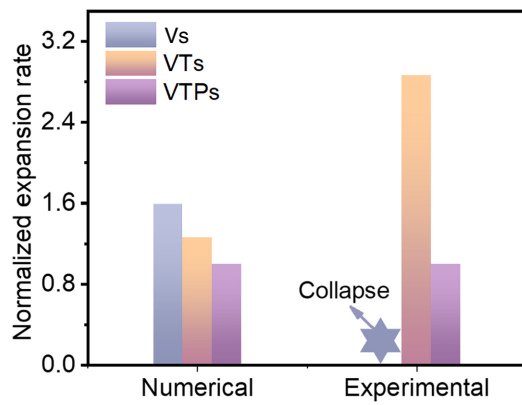
FIG. 10. Numerical and experimental expansion rate normalized by VTPs of Vs, VTs, and VTPs.

the V_2O_5 layer of VTs is still at risk of rupture because the radial stress in this case actually increases [Figs. 9(d) and 9(e)]. For VTPs, the radial stress and tangential stress of the PPy layer are larger than those in the V_2O_5 layer [Figs. 9(f) and 9(i)], which shows that the presence of an outer layer can effectively inhibit the expansion of the inner V_2O_5 layer. Meanwhile, the radial stress and tangential press in the V_2O_5 of VTPs are the lowest compared with those in Vs and VTPs, resulting in a highly stable structure during lithiation [Figs. 18(e) and 18(f) in Appendix B].
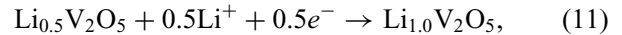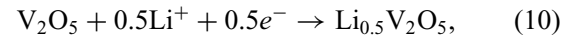
In summary, our results indicate that combining an internal support material and external coating material is more effective in improving the overall mechanical properties of the electrode and inhibiting expansion during lithiation, compared with using a single modification layer or relying solely on pure active materials.

Figure 10 illustrates the numerical and experimental normalized expansion rates of Vs, VTs, and VTPs. The numerical normalized expansion rates for Vs, VTs, and VTPs were found to be 159.31%, 126.16%, and 100.00%, respectively. Additionally, our analysis of the samples' volume change during the lithiation process revealed that the most significant volume change in Vs led to nanostructure breakage [47] while the volume change trend for VTs (286.58%) and VTPs (100.00%) was consistent with the numerical results [Fig. 10]. The congruence between the numerical and experimental outcomes confirms the effectiveness of the DHEMM approach in improving electrode stability.

C. Electrochemical performance

The electrochemical test results further confirm that the structural stability of VTPs is greatly enhanced during the charge and discharge cycle. The cyclic voltammograms of VTP cells have three obvious reduction peaks in first cycle [Fig. 11(a)]: 3.38, 3.17, and 2.27 V (versus Li/Li$^+$ redox couple), in accordance with the phase transformations from α-V_2O_5 to ε-$Li_{0.5}V_2O_5$, δ-$Li_{1.0}V_2O_5$, and

γ-$Li_{2.0}V_2O_5$, respectively [51]. The intercalation of the first Li occurs in two steps [52],

$$V_2O_5 + 0.5Li^+ + 0.5e^- \rightarrow Li_{0.5}V_2O_5, \qquad (10)$$

$$Li_{0.5}V_2O_5 + 0.5Li^+ + 0.5e^- \rightarrow Li_{1.0}V_2O_5, \qquad (11)$$

in good agreement with the cathodic peaks at 3.38 and 3.17 V. The cathodic peaks at 2.27 V demonstrate the intercalation of the second lithium ion through the reaction

$$Li_{1.0}V_2O_5 + 1.0Li^+ + 1.0e^- \rightarrow Li_{2.0}V_2O_5. \qquad (12)$$
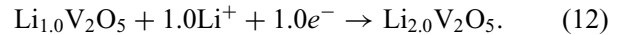
Three pairs of cathodic and anodic peaks corresponding to the other two electrodes (Vs, VTs) appear at 3.37/3.44, 3.17/3.25, 2.25/2.56 V and 3.38/3.43, 3.18/3.24, 2.29/2.43 V [Figs. 19(a) and 19(b) in Appendix B], indicating their lithium ions' deembedding behavior is similar to that of the VTPs. The cyclic voltammetry profiles of Vs demonstrate gradually weaker oxidation-reduction current during the three cycles due to the destruction of the electrode material [Fig. 19(a) in Appendix B]. However, the modification with the high-elastic-modulus protective layer in VTs and VTPs prevent significant changes in their oxidation-reduction current during the three cycles, verifying their superior structural stability compared to Vs. Compared to the poor capacity residual ratio of Vs [Fig. 19(c) in Appendix B] and VTs [Fig. 19(d) in Appendix B], the charge and discharge curves for the 50th and 100th cycles overlap with each other for VTPs [Fig 11(b)], indicating its good cycling stability over prolonged cycling.

EIS [Fig. 11(d)] illustrates that the charge-transfer resistance of VTPs (124.9 Ω) is lower than that of VTs (141.1 Ω) and Vs (615.6 Ω). Adding TiO$_2$ can prevent the aggregation of V_2O_5 nanoparticles and preserve a more electroactive surface, thereby contributing to the lower charge-transfer resistance observed for the VT electrode. Additionally, the PPy coating increases the conductivity of the materials, so VTPs can exhibit enhanced electrode reaction kinetics and high rate performance [41]. In order to observe the rate performance of the three samples, cells were tested from 100 mA g^{-1} to 1600 mA g^{-1} and back to 100 mA g^{-1} [Figs. 11(c) and 11(e)]. The capacity of the VTPs was approximately 198.2 mAh g^{-1} at 1600 mA g^{-1} and 259.7 mAh g^{-1} back to 100 mA g^{-1}, showing the best rate performance. The capacity of Vs and VTs was 5.6 mAh g^{-1} [Fig. 11(e) in Appendix B] and 145.6 mAh g^{-1} at 1600 mA g^{-1} [Fig. 11(e) in Appendix B], respectively, which indicates a poor rate performance consistent with the EIS.

After 100 cycles at a current density of 100 mA g^{-1}, the VTPs demonstrated a capacity retention of 253.7 mAh g^{-1}, which means 91.9% of their initial capacity of 276.1 mAh g^{-1} was preserved, as depicted in Fig. 11(f). This suggests an enhanced structural stability of VTPs, as substantiated
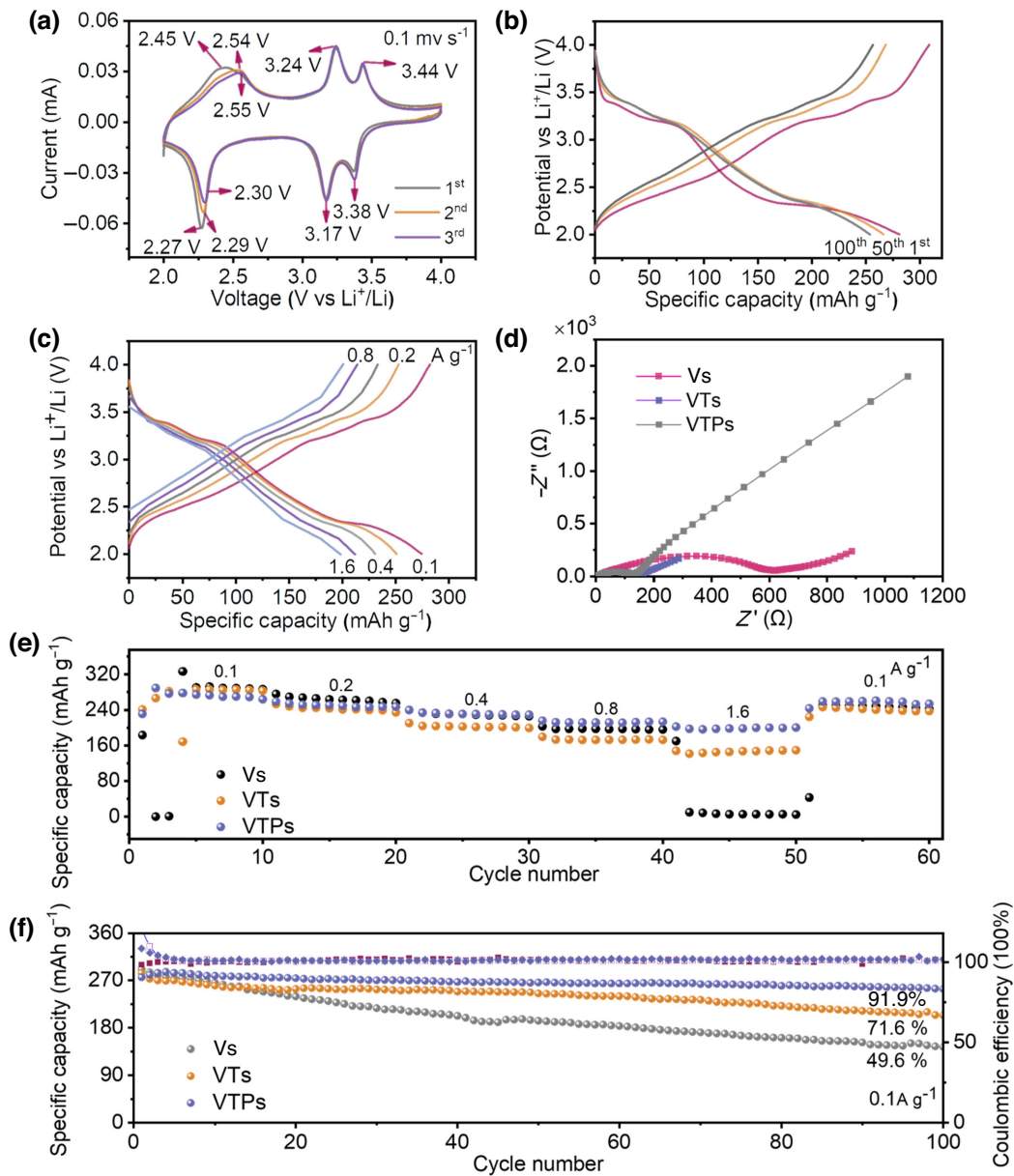
FIG. 11. (a) Cyclic voltammograms of first, second, third cycles of samples at a scan rate of 0.1 mV s^{-1}, (b) galvanostatic charge-discharge (GCD) profiles of first, 50th, 100th cycles at 0.1 A g^{-1} of VTPs and (c) GCD profiles of various current densities from 0.1 to 1.6 A g^{-1} of VTPs. (d) Nyquist plots of Vs, VTs, and VTPs. (e) Rate performances of Vs, VTs, and VTPs from 0.1 to 1.6 A g^{-1}. (f) Cycling performance of *V*, VT, and VTP cells at a current density of 100 mA g^{-1} between 2.0 and 4.0 V.

by their well-maintained morphology with distinct lattice fringes of V$_2$O$_5$ and the PPy coating layer even after 100 cycles, as observed in Figs. 20(a)–20(c) in Appendix B. In contrast, Vs and VTs showed disrupted fiber morphology with no visible lattice striping after 100 cycles, as depicted in Figs. 20(d)–20(i) in Appendix B. Consequently, Vs and VTs experienced a faster decline in capacity in comparison to VTPs, with decay rates of 49.6% and 71.6%, respectively, of their initial capacity, as illustrated in Fig. 11(f).

V. CONCLUSION

In this research, we utilized a lithium-ion diffusion model to investigate the impact of different modulus distributions in a trilayer material on DIS and deformation of active materials during lithiation. Based on our findings, we proposed that an active material with inner and outer high-modulus protection layers can suffer smaller DIS and deformation during lithiation and improve the structural stability of electrode. With the DHEMM strategy as a guide, the VTPs, which have an inner TiO$_2$ layer and outer
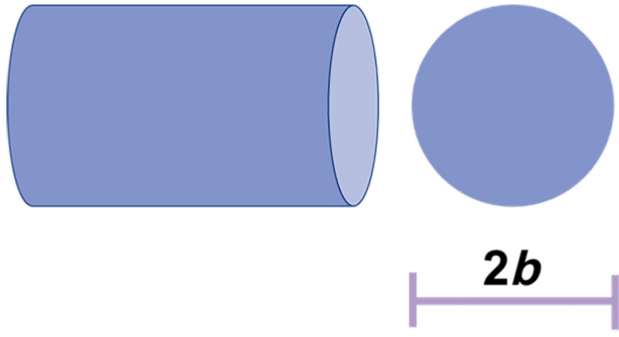
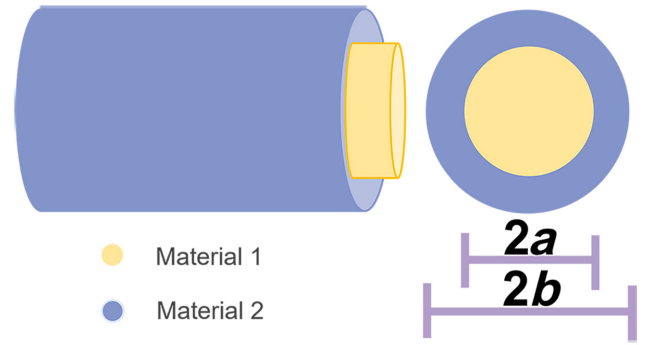FIG. 12.   Schematic of a single-layer nanofiber.

FIG. 13.   Schematic of a two-layer nanofiber.

PPy coating layer as high-modulus modifications, exhibit the lowest diameter change compared to materials without any protective layer modification (Vs) or those only with a single high-modulus protective inner layer (VTs) after lithiation. Simulation analysis for Vs, VTs, and VTPs indicated that an outer PPy coating and an inner TiO_2 layer on the V_2O_5 layer effectively suppressed both radial and tangential stresses, resulting in minimal deformation during charge and discharge. Hence, the VTP electrode exhibited a stable structure and enhanced cycling stability with a high capacity retention rate of 91.9% after 100 cycles at a current density of 100 mA g^{-1}.

Simulation and experimental findings indicate that the design of a trilayer structure based on DHEMM can achieve structural stability of electrodes. This provides guidance for the development of protective composites that reduce the deformation and DIS of electrodes during lithiation. Specifically, it is enlightening in the design of electrode materials such as SiO_2 and SnO_2, which experience notable alterations in volume during the process of lithiation.

APPENDIX A: DETAILED MATHEMATICAL PROCESS

List of symbols

Symbol	Description (Units)
r, θ, z	Cylindrical coordinates
σ_r	Radial stress (Nm^{-2})
σ_θ	Tangential stress (Nm^{-2})
σ_z	Body stress (Nm^{-2})
σ_h	Hydrostatic pressure (Nm^{-2})
E	Young's modulus (Nm^{-2})
ν	Poisson's ratio
ε_r	Radial strain
ε_θ	Tangential strain
Ω	Partial molar volumes ($m^3 mol^{-1}$)
C	Concentration ($mol m^{-3}$)
C_{avgi}	Average concentration in component i ($mol m^{-3}$)
u	Displacement (m)
r	Radius (m)
S_θ	Surface/interface stress (Nm^{-2})
τ	Deformation-independent residual surface/ interface stress (Nm^{-2})
λ_s and μ_s	Surface Lamé constants (Nm^{-1})
K	Surface/interface modulus
μ	Chemical potential ($KJ mol^{-1}$)
R	Gas constant ($J mol^{-1} K^{-1}$)
T	Absolute temperature (K)
X	Molar fraction of lithium ion
$\overrightarrow{J}$	Lithium-ion flux ($mol m^{-2} s^{-1}$)
M	Mobility of lithium ions
D	Diffusion coefficient ($cm^2 s^{-1}$)
J_s	Surface lithium-ion flux ($mol m^{-2} s^{-1}$)

As shown in Fig. 12, mechanical equilibrium can be treated as a static equilibrium problem because mechanical equilibrium is reached more quickly than diffusion equilibrium. The stress components must satisfy the equilibrium equation if body force is neglected [22],

$$\frac{d\sigma_r}{dr} + \frac{2(\sigma_r - \sigma_\theta)}{r} = 0. \tag{A1}$$

Considering the influence of lithium-ion concentration, constitutive equations of the two stress components in the cylindrical coordinate system can be written as [53]

$$\sigma_r = \frac{E}{(1-\nu)(1+\nu)}\left[\varepsilon_r + \nu\varepsilon_\theta - (1+\nu)\frac{\Omega}{3}C\right],$$

$$\sigma_\theta = \frac{E}{(1-\nu)(1+\nu)}\left[\varepsilon_\theta + \nu\varepsilon_r - (1+\nu)\frac{\Omega}{3}C\right]. \tag{A2}$$

Under the small-deformation hypothesis, radial strain ε_r and tangential strain ε_θ can be expressed in terms of displacement u,

$$\varepsilon_r = \frac{du}{dr}, \quad \varepsilon_\theta = \frac{u}{r}. \tag{A3}$$

Substituting Eqs. (A3) and (A2) into (A1), the differential equation for u can be written as

$$r^2\frac{d^2u}{dr^2} + r\frac{du}{dr} - u = (1+v)\frac{\Omega}{3}r^2\frac{dC}{dr}. \tag{A4}$$

The analytical form of displacement u can easily be obtained using the Euler equation

$$u = (1+v)\frac{\Omega}{3}\frac{1}{r}\int_{r_i}^{r} Crdr + \frac{A}{r} + Br. \tag{A5}$$

The constants, A and B can be determined later by boundary conditions. Substituting Eqs. (A4) and (A2) into (A1), the analytical form of the two stress components can be written as

$$\sigma_r = -\frac{\Omega}{3}E\frac{1}{r^2}\int_{r_0}^{r} Crdr - \frac{E}{1+v}\frac{A}{r^2} + \frac{E}{1-v}B,$$

$$\sigma_\theta = \frac{\Omega}{3}E\frac{1}{r^2}\int_{r_0}^{r} Crdr - \frac{\Omega}{3}EC + \frac{E}{1+v}\frac{A}{r^2} + \frac{E}{1-v}B. \tag{A6}$$

We can obtain the analytical form of the two strain components using Eqs. (A3) and (A5) and (A6),

$$\varepsilon_r = (1+v)\frac{\Omega}{3}\left(-\frac{1}{r^2}\int_{r_0}^{r} Crdr + C\right) - \frac{A}{r^2} + B,$$

$$\varepsilon_\theta = (1+v)\frac{\Omega}{3}\frac{1}{r^2}\int_{r_0}^{r} Crdr + \frac{A}{r^2} + B. \tag{A7}$$

For a two-layer cylinder, as shown in Fig. 13, there should be four constants determined by boundary conditions,
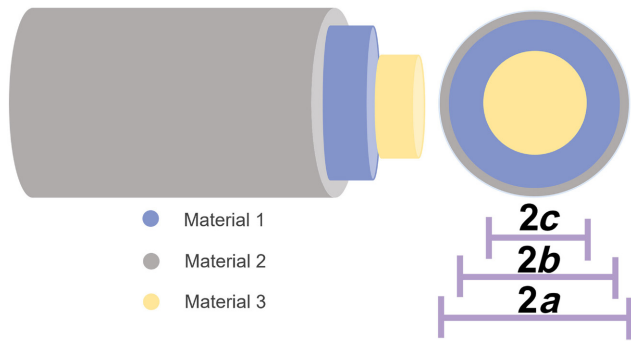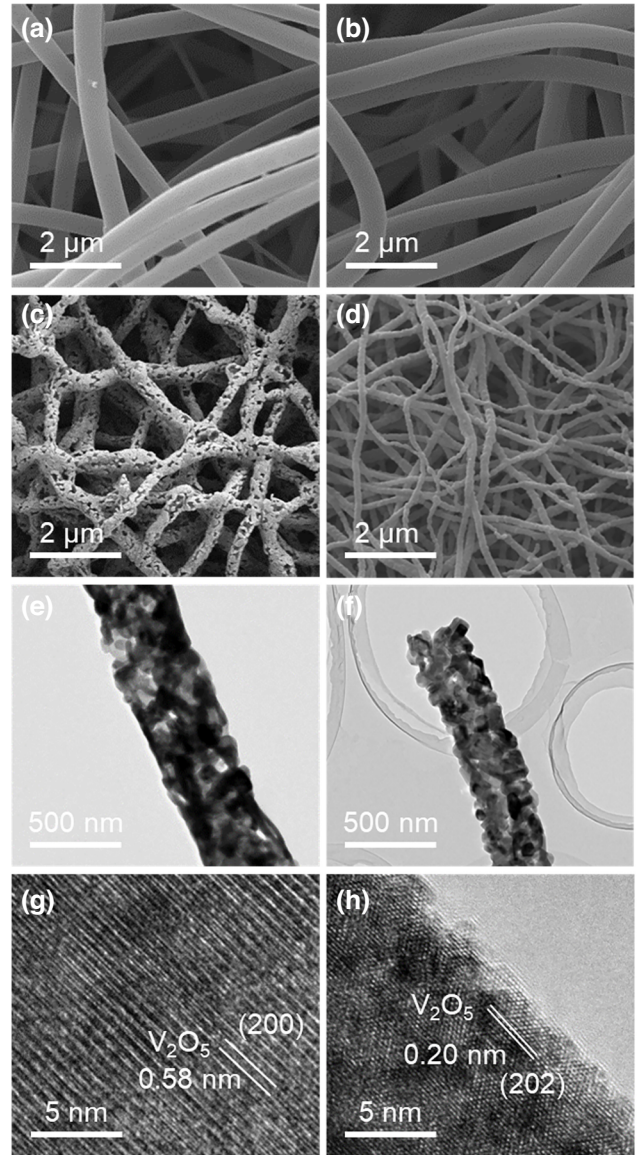

FIG. 14. Schematic of trilayer nanofiber.

FIG. 15. SEM images of as-spun (a) Vs and (b) VTs, sintered (c) Vs and (d) VTs. TEM images of (e) Vs and (f) VTs. HRTEM of (g) Vs and (h) VTs.

namely A_1 and B_1 in material 1 and A_2 and B_2 in material 2. Note that the whole material is fixed on the current collector, which indicates $u = 0$ at $r = 0$.

In this case, there are two boundaries to consider, which are the interface between the core material and shell material at $r = a$ and the surface between shell material and electrolyte at $r = b$. Here we have a surface stress-strain constitutive relationship. For isotropic elastic surfaces/interfaces, we have [22],

$$S_\theta = \tau + 2(\lambda_s + \mu_s)\left(\varepsilon_\theta - \frac{\Omega C}{3}\right) = \tau + K\left(\varepsilon_\theta - \frac{\Omega C}{3}\right), \tag{A8}$$
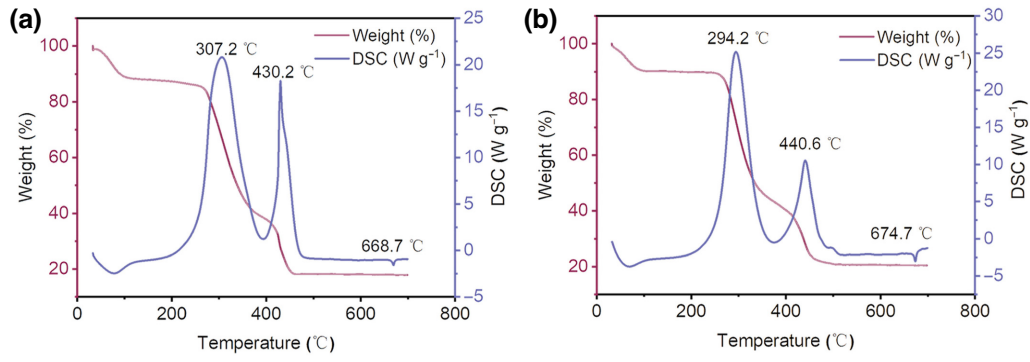
FIG. 16.   TG DSC profiles of (a) Vs and (b) VTs in air.

where S_θ is surface stress, λ_s and μ_s are the surface Lamé constants, K can be defined as surface/interface modulus, and τ is the deformation-independent residual surface/interface stress. The term $\Omega C/3$ in the equation mainly reflects the strain (material expansion) caused by ion insertion.

At the outer surface, radial stress must satisfy the machine mechanical equilibrium [22],

$$\sigma_r|_{r=b} = -\frac{2S_\theta|_{r=b}}{b}. \tag{A9}$$

In this case, we assume the materials are perfectly bounded at the interface. Hence, for the interface between two materials, deformation and the two components of strain should be continuous,

$$u_1|_{r=a} = u_2|_{r=a}. \tag{A10}$$

In order to obey the generalized Young-Laplace equation [22], there should be a pressure difference on each side of the interface where the two materials are in contact, so there should be a sudden change in the radial stress at the interface, and we have

$$\sigma_{1r}|_{r=a} - \sigma_{2r}|_{r=a} = -\frac{2S_\theta|_{r=a}}{a}. \tag{A11}$$

From Eqs. (A9)–(A11), we can obtain the three constants B_1, A_2, and B_2. Using Eqs. (A5)–(A8), we can obtain a group of linear equations as follows:

$$
\begin{pmatrix}
1 & -1 & -\dfrac{1}{a^2} \\[2ex]
0 & \dfrac{1}{1-\nu_2} + \dfrac{2K_2}{bE_2} & \left(-\dfrac{1}{1+\nu_2} + \dfrac{2K_2}{bE_2}\right)\dfrac{1}{b^2} \\[2ex]
\dfrac{1}{1-\nu_1} + \dfrac{2K_1}{aE_1} & -\dfrac{1}{1-\nu_2}\dfrac{E_2}{E_1} & \dfrac{1}{1+\nu_2}\dfrac{E_2}{E_1}\dfrac{1}{a^2}
\end{pmatrix}
\begin{pmatrix} B_1 \\[2ex] B_2 \\[2ex] A_2 \end{pmatrix}
$$

$$
=
\begin{pmatrix}
-(1+\nu_1)\dfrac{\Omega_1 C_{\text{avg1}}}{6} \\[2ex]
\dfrac{\Omega_2 C_{\text{avg2}}}{6}\left[1 - \dfrac{2K_2}{bE_2}(1+\nu_2)\right] - \dfrac{2}{bE_2}\left(\tau_2 - \dfrac{K_2\Omega_2 C|_{r=b}}{3}\right) \\[2ex]
\dfrac{\Omega_1 C_{\text{avg1}}}{6}\left[1 - \dfrac{2K_1}{aE_1}(1+\nu_1)\right] - \dfrac{2}{aE_1}\left(\tau_1 - \dfrac{K_1\Omega_1 C|_{r=a}}{3}\right)
\end{pmatrix}, A_1 = 0, \tag{A12}
$$

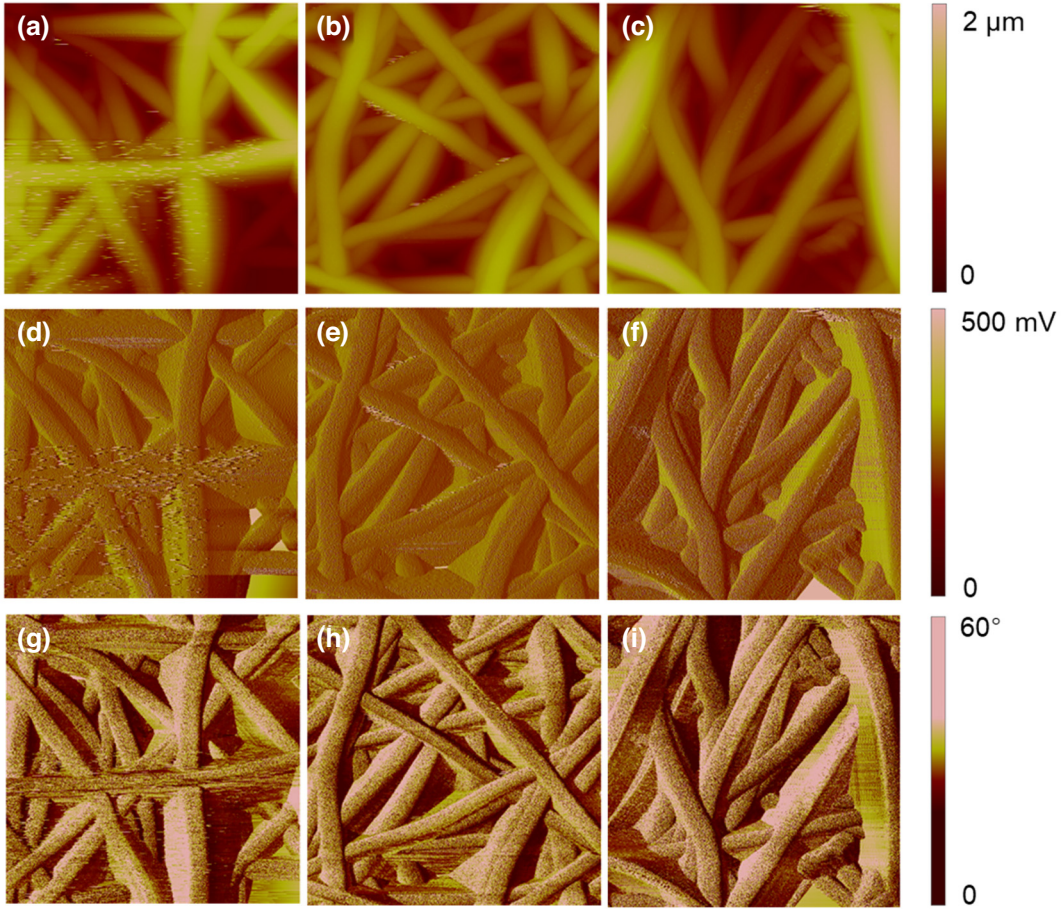where $C_{\text{avg}}(r) = (2/r^2)\int_0^r C(r')r'\,dr'$.[15]

FIG. 17.   AFM topography of (a) Vs, (b) VTs, and (c) VTPs. Deflection error images of (d) Vs, (e) VTs, and (f) VTPs. SPAM phase images of (g) Vs, (h) VTs, and (i) VTPs.

It is clear that B_1, A_2, and B_2 depend on the following five dimensionless constants: (K_2/bE_2) and (τ_2/bE_2), which mainly describe the surface stress at the interface between the outer surface of the material and the electrolyte, and (K_1/aE_1), (τ_1/aE_1), and (E_2/E_1), which mainly describe the surface stress between material 1 and material 2. Since the surface modulus K and residual surface stress τ can be either positive or negative, their values do not influence the curve shape but only the signs. Hence, we simply set $K = \pm 10$ N/m and $\tau = \pm 0.2$ N/m in order to ensure the rationality of the results [22], which

TABLE IV.   Element ratio of VTs.

Element	Wt %	At %
C	88.95	92.41
O	9.12	7.11
Ti	0.31	0.08
V	1.61	0.40

are applied to the calculation of the following trilayer structure.

Consider a cylinder with a trilayer structure as shown in Fig. 14: we have six boundary-dependent constants, namely A_1, B_1 in material 1, A_2, B_2 in material 2, and A_3, B_3 in material 3. Correspondingly there should be three boundaries. Based on the previous argument, $A_3 = 0$, and the boundary conditions can be written as,

$$\sigma_r|_{r=b} = -\frac{2S_\theta|_{r=b}}{b},$$

$$u_1|_{r=a} = u_2|_{r=a},$$

$$\sigma_{1r}|_{r=a} - \sigma_{2r}|_{r=a} = -\frac{2S_\theta|_{r=a}}{a},$$

$$u_3|_{r=c} = u_1|_{r=c},$$

$$\sigma_{3r}|_{r=c} - \sigma_{1r}|_{r=c} = -\frac{2S_\theta|_{r=c}}{c}, \tag{A13}$$
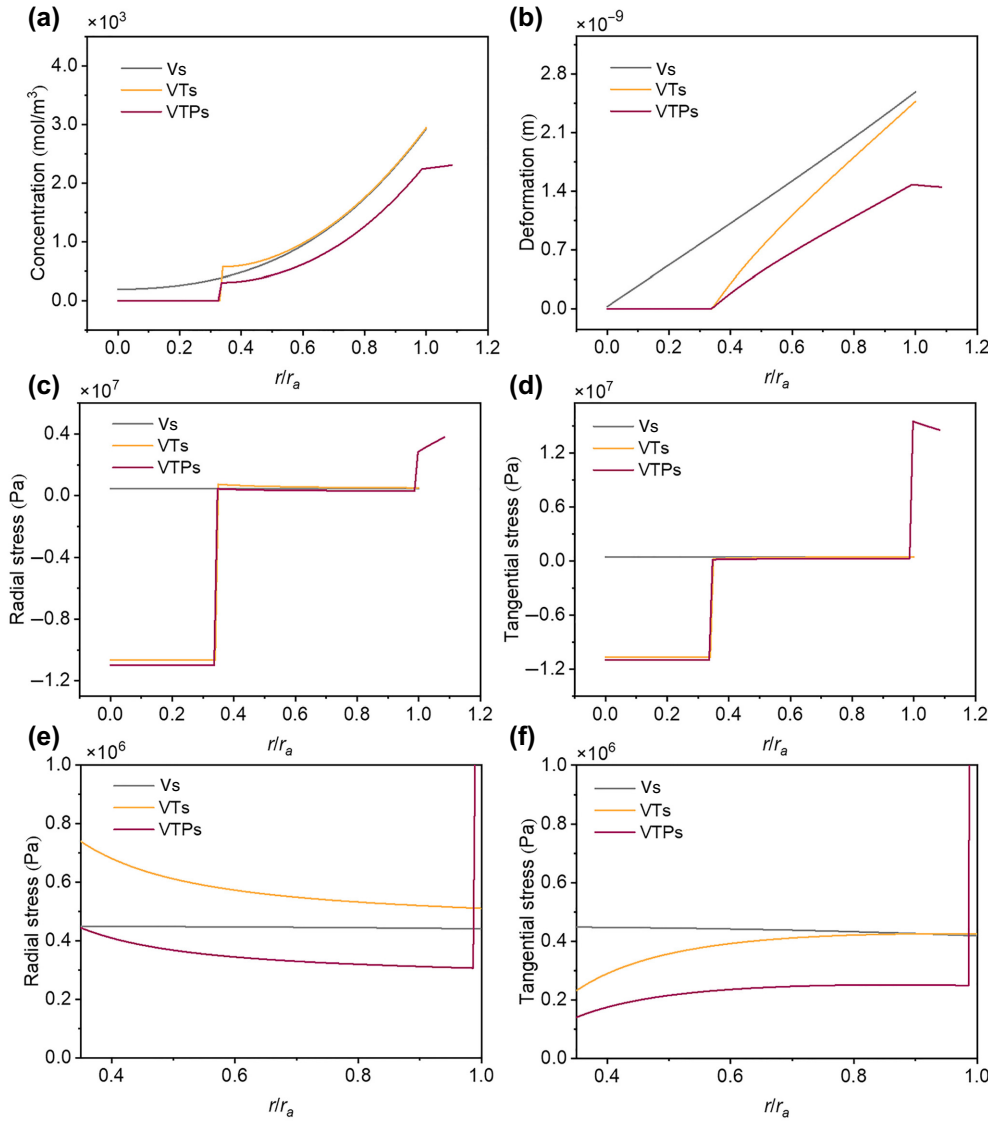
which is

FIG. 18. Radial distribution curves of (a) lithium-ion concentration, (b) deformation, (c),(e) radial stress, (d),(f) tangential stress.

$$\begin{pmatrix} 1 & -1 & \frac{1}{a^2} & -\frac{1}{a^2} & 0 \\ 0 & \frac{1}{1-\nu_2} + \frac{2K_2}{bE_2} & 0 & \left(-\frac{1}{1+\nu_2} + \frac{2K_2}{bE_2}\right)\frac{1}{b^2} & 0 \\ \frac{1}{1-\nu_1} + \frac{2K_1}{aE_1} & -\frac{1}{1-\nu_2}\frac{E_2}{E_1} & \left(\frac{2K_1}{aE_1} - \frac{1}{1+\nu_1}\right)\frac{1}{a^2} & \frac{1}{1+\nu_2}\frac{E_2}{E_1}\frac{1}{a^2} & 0 \\ -1 & 0 & -\frac{1}{c^2} & 0 & 1 \\ -\frac{1}{1-\nu_1}\frac{E_1}{E_3} & 0 & \frac{1}{1+\nu_1}\frac{E_1}{E_3}\frac{1}{c^2} & 0 & \frac{1}{1-\nu_3} + \frac{2K_3}{cE_3} \end{pmatrix} \begin{pmatrix} B_1 \\ B_2 \\ A_1 \\ A_2 \\ B_3 \end{pmatrix}$$

$$= \begin{pmatrix} -(1+\nu_1)\frac{\Omega_1 C_{\text{avg}1}}{6} \\ \frac{\Omega_2 C_{\text{avg}2}}{6}\left[1 - \frac{2K_2}{bE_2}(1+\nu_2)\right] - \frac{2}{bE_2}\left(\tau_2 - \frac{K_2\Omega_2 C|_{r=b}}{3}\right) \\ \frac{\Omega_1 C_{\text{avg}1}}{6}\left[1 - \frac{2K_1}{aE_1}(1+\nu_1)\right] - \frac{2}{aE_1}\left(\tau_1 - \frac{K_1\Omega_1 C|_{r=a}}{3}\right) \\ -(1+\nu_3)\frac{\Omega_3 C_{\text{avg}3}}{6} \\ \frac{\Omega_3 C_{\text{avg}3}}{6}\left[1 - \frac{2K_3}{cE_3}(1+\nu_3)\right] - \frac{2}{cE_3}\left(\tau_3 - \frac{K_3\Omega_3 C|_{r=c}}{3}\right) \end{pmatrix},$$
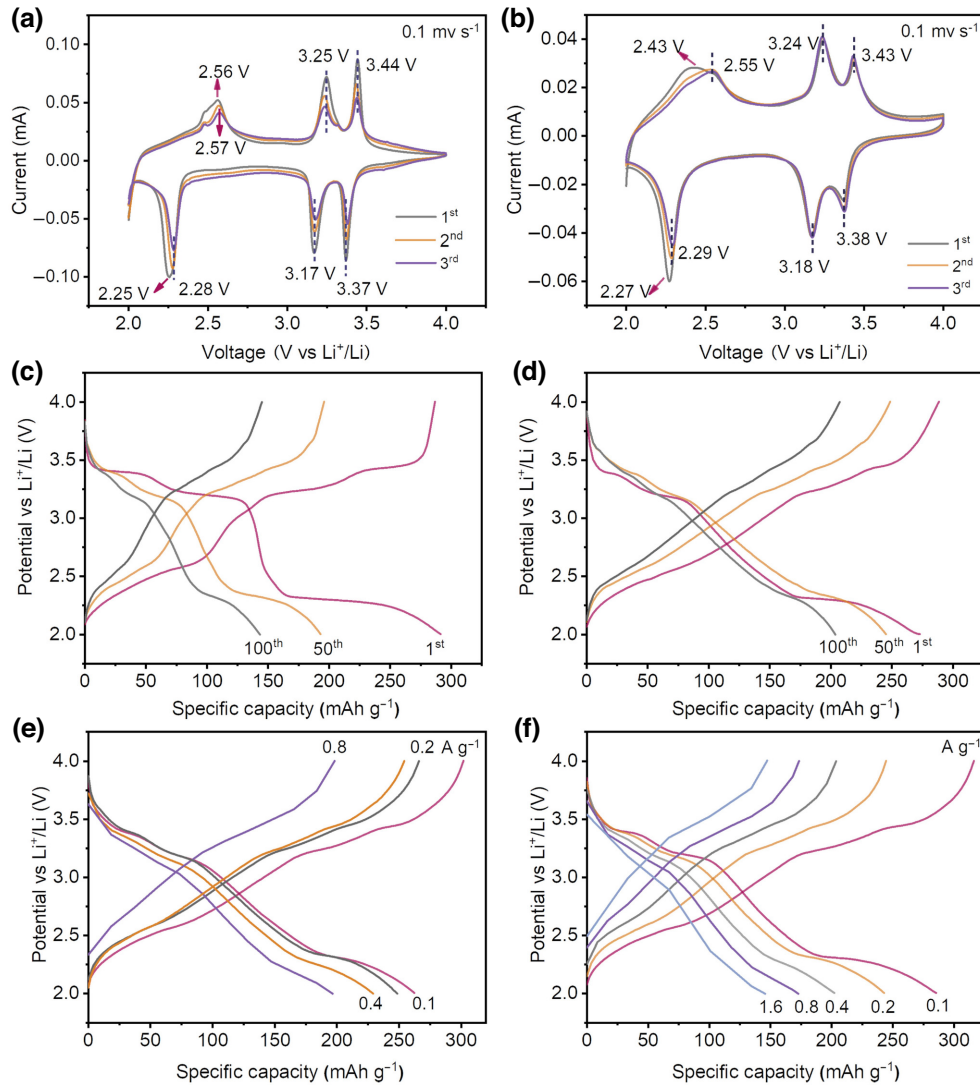
$$A_3 = 0. \tag{A14}$$

FIG. 19.   Cyclic voltammograms of first, second, third cycles of (a) V and (b) VT cells at a scan rate of 0.1 mV s^{-1}. Galvanostatic charge-discharge (GCD) profiles of first, 50th, 100th cycles of (c) V, (d) VT cells at 0.1 A g^{-1}. GCD profiles of various current densities from 0.1 to 1.6 A g^{-1} of (e) V and (f) VT cells between 2 and 4 V.

Diffusion equation

As the driving force of lithium-ion diffusion, the chemical potential μ in an ideal solid solution can be written as [54]

$$\mu = \mu_0 + RT \ln X - \Omega \sigma_h, \qquad (A15)$$

in which μ is the chemical potential, μ_0 is a constant, R is the gas constant, T is the absolute temperature, X is the molar fraction of lithium ions, and σ_h is the hydrostatic pressure.

Axial stress σ_z can be considered to be zero because of the generalized plane strain condition. Hence, hydrostatic pressure can be written as,

$$\sigma_h = \frac{1}{3}(\sigma_r + \sigma_\theta + \sigma_z) = \frac{E}{3(1-\nu)} \left(\varepsilon_r + \varepsilon_\theta - \frac{2}{3} \Omega C \right)$$
$$= -\frac{\Omega}{9} EC + \frac{2EB}{3(1-\nu)}. \qquad (A16)$$

Hence, the diffusion flux of lithium ions can be written as [19]

$$\vec{J} = -MC\nabla\mu. \qquad (A17)$$

From the definition of the diffusion coefficient, we have
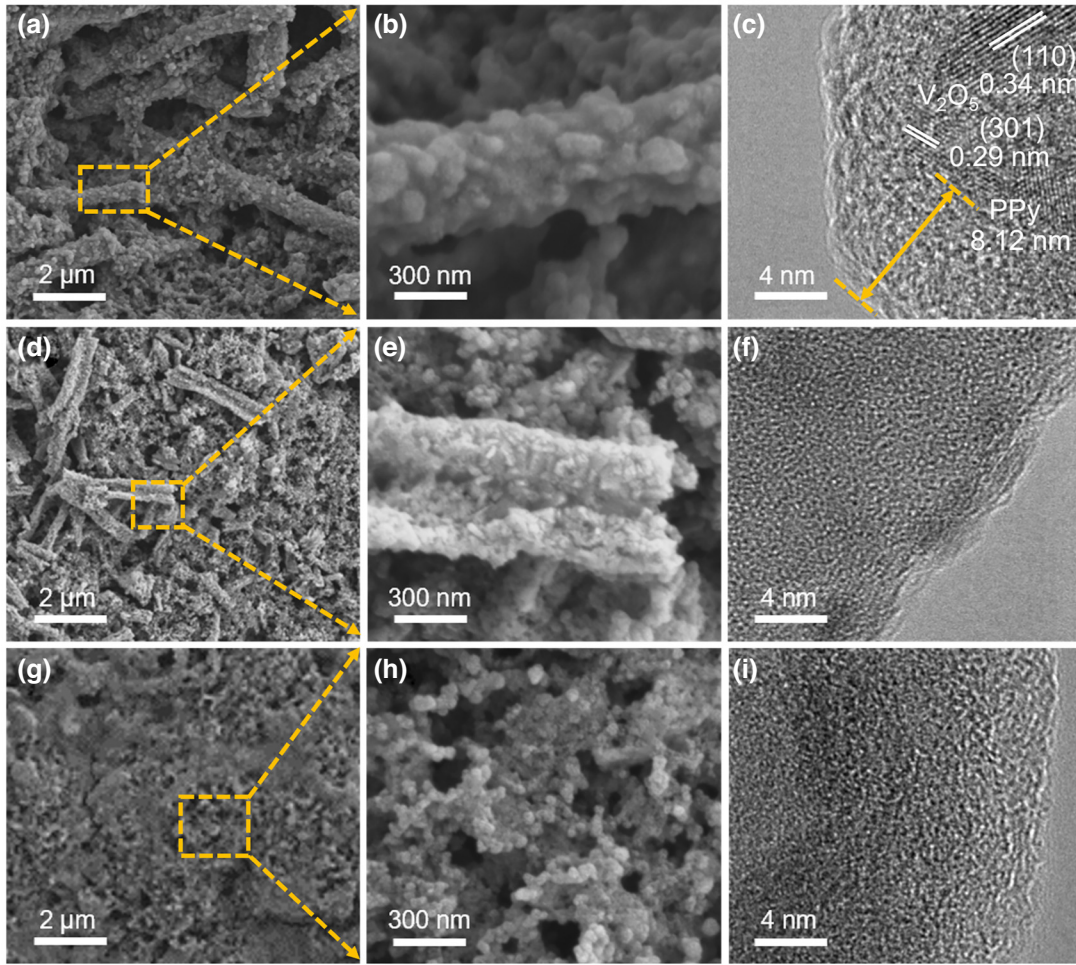
$$D = MRT. \qquad (A18)$$

FIG. 20.   SEM images of (a),(b) VTPs, (d),(e) VTs, and (g),(h) Vs after 100 cycles. HRTEM images of (c) VTPs, (f) VTs, and (i) Vs after 100 cycles.

Combining Eqs. (A15) and (A17), diffusion flux can be written as

$$\vec{J} = -D\left(\nabla C - \frac{\Omega C}{RT}\nabla\sigma_h\right) = -D\left[\left(1 + \frac{\Omega^2 C}{9RT}E\right)\nabla C\right],$$
$$(A19)$$

where $(\Omega^2 E)/(9RT)$ is a positive constant that reflects the effect of hydrostatic pressure on the diffusion flux. Owing to the constant current condition, the initial condition can be written in the following form [19]:

$$\frac{\partial C}{\partial t} + \nabla \cdot \vec{J} = 0. \qquad (A20)$$

If we let $\theta = (\Omega^2 E)/(9RT)$, we have

$$\frac{\partial C}{\partial t} = D\left[(1 + \theta C)\frac{\partial^2 C}{\partial r^2} + \frac{2}{r}(1 + \theta C)\frac{\partial C}{\partial r} + \theta\left(\frac{\partial C}{\partial r}\right)^2\right].$$
$$(A21)$$

Owing to the constant current condition, the initial condition can be written in the following form:

$$\begin{aligned}C(r, t = 0) &= C_0,\\ D(1 + \theta C)\tfrac{\partial}{\partial r}C(r = 0, t) &= 0,\\ D(1 + \theta C)\tfrac{\partial}{\partial r}C(r = b, t) &= \vec{J_s}.\end{aligned} \qquad (A22)$$

In addition, to satisfy the continuity condition, for a two-layer cylinder [22],

$$\begin{aligned}C_1(r = a, t) &= C_2(r = a, t),\\ \vec{J_1}(r = a, t) &= \vec{J_2}(r = a, t).\end{aligned} \qquad (A23)$$

For a trilayer structure, we add one more boundary condition,

$$\begin{aligned}C_3(r = a, t) &= C_1(r = a, t),\\ \vec{J_3}(r = a, t) &= \vec{J_1}(r = a, t).\end{aligned} \qquad (A24)$$

Likewise, we can obtain other boundary conditions to acquire the constants A and B. Obviously, it is difficult

to obtain an analytical solution to the equations above. To solve these nonlinear equations, the finite-difference method is applied. Additionally, time and location need to be discretized. In addition to the several mechanical properties of the material itself and the diffusion characteristics of lithium ions, DIS also depends on the charging current density J_s, charging time (diffusion time) , surface modulus K, and residual surface stress τ based on the previous discussion. For the charging current density J_s, we can simplify the calculations using a dimensionless treatment. In the following discussions, the dimensionless current density $j_u = (J_s b)/(D_1 C_{1\,\max})$ is introduced. When $j_u = 0.25$, the actual current density can be calculated by the specific material properties. Under this condition, the number of lithium ions in the nanofiber remains 4.50×10^{-11} mol per unit length.

APPENDIX B: MORE DATA FOR Vs, VTs, AND VTPs

Figure 15 shows SEM images of as-spun and sintered Vs, VTs, along with TEM, and HRTEM images of Vs, VTs. Figure 16 shows TG-DSC profiles of Vs and VTs in air. Figure 17 shows AFM topography, deflection error images and SPAM phase images of Vs, VTs and VTPs. Figure 18 displays the simulation results depicting the radial distribution of lithium-ion concentration, deformation, radial stress, and tangential stress of Vs, VTs, and VTPs. Figure 19 displays electrochemical properties of V and VT cells, which includes cyclic voltammograms and GCD profiles. Figure 20 shows SEM and HRTEM images of Vs, VTs and VTPs after 100 cycles. We use EDS to obtain the element ratio of VTs. Specific element ratio of C, O, Ti and V is shown in Table IV.

---

[1] A. Yoshino, The birth of the lithium-ion battery, Angew. Chem., Int. Ed. **51**, 5798 (2012).

[2] Q. Xie, Z. Cui, and A. Manthiram, Unveiling the stabilities of nickel-based layered oxide cathodes at an identical degree of delithiation in lithium-based batteries, Adv. Mater. **33**, 2100804 (2021).

[3] H. Pourfarzad, M. Shabani-Nooshabadi, and M. R. Ganjali, High lithium anodic performance of reduced Sn particles on Co metal-organic frameworks for lithium-ion batteries with a long-cycle life, Composites, Part B **193**, 108008 (2020).

[4] E. Markervich, G. Salitra, M. D. Levi, and D. Aurbach, Capacity fading of lithiated graphite electrodes studied by a combination of electroanalytical methods, Raman spectroscopy and SEM, J. Power Sources **146**, 146 (2005).

[5] H. Wang, Y. I. Jang, B. Huang, D. R. Sadoway, and Y. M. Chiang, TEM study of electrochemical cycling-induced damage and disorder in LiCoO$_2$ cathodes for rechargeable lithium batteries, J. Electrochem. Soc. **146**, 473 (1999).

[6] M.-R. Lim, W.-I. Cho, and K.-B. Kim, Preparation and characterization of gold-codeposited LiMn$_2$O$_4$ electrodes, J. Power Sources **92**, 168 (2001).

[7] H. Gabrisch, J. Wilcox, and M. M. Doeff, TEM study of fracturing in spherical and plate-like LiFePO$_4$ particles, Electrochem. Solid-State Lett. **11**, A25 (2007).

[8] K. Zhang, Y. Li, and B. Zheng, Effects of concentration-dependent elastic modulus on Li-ions diffusion and diffusion-induced stresses in spherical composition-gradient electrodes, J. Appl. Phys. **118**, 105102 (2015).

[9] H. Bai, Z. Liu, D. D. Sun, and S. H. Chan, Hierarchical 3D micro-/nano-V$_2$O$_5$ (vanadium pentoxide) spheres as cathode materials for high-energy and high-power lithium ion-batteries, Energy **76**, 607 (2014).

[10] M. Chen, X. Xia, J. Yuan, J. Yin, and Q. Chen, Free-standing three-dimensional continuous multilayer V$_2$O$_5$ hollow sphere arrays as high-performance cathode for lithium batteries, J. Power Sources **288**, 145 (2015).

[11] G.-L. Xu, Q. Liu, K. K. S. Lau, Y. Liu, X. Liu, H. Gao, X. Zhou, M. Zhuang, Y. Ren, J. Li, M. Shao, M. Ouyang, F. Pan, Z. Chen, K. Amine, and G. Chen, Building ultra-conformal protective layers on both secondary and primary particles of layered lithium transition metal oxide cathodes, Nat. Energy **4**, 484 (2019).

[12] X. Liang, G. Gao, X. Jiang, W. Zhang, W. Bi, J. Wang, Y. Du, and G. Wu, Preparation of hydrophobic PPy coated V$_2$O$_5$ yolk–shell nanospheres-based cathode materials with excellent cycling performance, ACS Appl. Energy Mater. **3**, 2791 (2020).

[13] K.-J. Park, H.-G. Jung, L.-Y. Kuo, P. Kaghazchi, C. S. Yoon, and Y.-K. Sun, Improved cycling stability of LiNi$_{0.90}$Co$_{0.05}$Mn$_{0.05}$O$_2$ through microstructure modification by boron doping for Li-ion batteries, Adv. Energy Mater. **8**, 1801202 (2018).

[14] H.-H. Ryu, K.-J. Park, D. R. Yoon, A. Aishova, C. S. Yoon, and Y.-K. Sun, LiNi$_{0.90}$Co$_{0.09}$W$_{0.01}$O$_2$: A new type of layered oxide cathode with high cycling stability, Adv. Energy Mater. **9**, 1970174 (2019).

[15] R. Deshpande, Y. T. Cheng, and M. W. Verbrugge, Modeling diffusion-induced stress in nanowire electrode structures, J. Power Sources **195**, 5081 (2010).

[16] M. T. Mcdowell, S. Xia, and T. Zhu, The mechanics of large-volume-change transformations in high-capacity battery materials, Extreme Mech. Lett. **9**, 480 (2016).

[17] S. Prussin, Generation and distribution of dislocations by solute diffusion, J. Appl. Phys. **32**, 1876 (1961).

[18] J. Christensen and J. Newman, Stress generation and fracture in lithium insertion materials, J. Solid State Electrochem. **10**, 293 (2006).

[19] X. Zhang, W. Shyy, and A. M. Sastry, Numerical simulation of intercalation-induced stress in Li-ion battery electrode particles, J. Electrochem. Soc. **154**, A910 (2007).

[20] L. Xu, W. Liu, Y. Hu, and L. Luo, Stress-resilient electrode materials for lithium-ion batteries: Strategies and mechanisms, Chem. Commun. **56**, 13301 (2020).

[21] F. Hao, X. Gao, and D. Fang, Diffusion-induced stresses of electrode nanomaterials in lithium-ion battery: The effects of surface stress, J. Appl. Phys. **112**, 103507 (2012).

[22] F. Hao and D. Fang, Diffusion-induced stresses of spherical core-shell electrodes in lithium-ion batteries: The effects of

the shell and surface/interface stress, J. Electrochem. Soc. **160,** A595 (2013).

[23] Y. T. Cheng and M. W. Verbrugge, The influence of surface mechanics on diffusion induced stresses within spherical nanoparticles, J. Appl. Phys. **104,** 083521 (2008).

[24] A. Ohashi, M. Kodama, N. Hofrikawa, and S. Hirai, Effect of Young's modulus of active materials on ion transport through solid electrolyte in all-solid-state lithium-ion battery, J. Power Sources **483,** 229212 (2021).

[25] H. B. Lin, H. B. Rong, W. Z. Huang, Y. H. Liao, L. D. Xing, M. Q. Xu, X. P. Li, and W. S. Li, Treble-shelled Mn_2O_3 hollow nanocubes: Force-induced synthesis and excellent performance as anode of lithium-ion battery, J. Mater. Chem. A **2,** 14189 (2014).

[26] L. Zu, Q. Su, F. Zhu, B. Chen, H. Lu, C. Peng, T. He, G. Du, P. He, K. Chen, S. Yang, J. Yang, and H. Peng, Antipulverization electrode based on low-carbon triple-shelled superstructures for lithium-ion batteries, Adv. Mater. **29,** 1701494 (2017).

[27] Y. Zhou, Z. Jia, S. Zhao, P. Chen, Y. Wang, T. Guo, L. Wei, X. Cui, X. Ouyang, X. Wang, J. Zhu, J. Sun, S. Pan, and Y. Fu, Construction of triple-shelled hollow nanostructure by confining amorphous Ni-Co-S/crystalline MnS on/in hollow carbon nanospheres for all-solid-state hybrid supercapacitors, Chem. Eng. J. **416,** 129500 (2021).

[28] Y. Lee, T. Lee, J. Hong, J. Sung, N. Kim, Y. Son, J. Ma, S. Y. Kim, and J. Cho, Stress relief principle of micronsized anodes with large volume variation for practical high-energy lithium-ion Batteries, Adv. Funct. Mater. **30,** 2004841 (2020).

[29] J. Sun, A. M. Forster, P. M. Johnson, N. Eidelman, G. Quinn, G. Schumacher, X. Zhang, and W. Wu, Improving performance of dental resins by adding titanium dioxide nanoparticles, Dent. Mater. **27,** 972 (2011).

[30] L. Noerochim, J. Z. Wang, D. Wexler, Md. M. Rahman, J. Chen, and H. K. Liu, Impact of mechanical bending on the electrochemical performance of bendable lithium batteries with paper-like free-standing V_2O_5–polypyrrole cathodes, J. Mater. Chem. **22,** 11159 (2012).

[31] See the Supplemental Material at http://link.aps.org/supplemental/10.1103/PhysRevApplied.20.024079 for schematics of electrospinning process and scanning probe acoustic microscope, and fiber diameter statistics of Vs, VTs, and VTPs.

[32] X. Z. Ren, C. Shi, P. X. Zhang, Y. K. Jiang, J. H. Liu, and Q. L. Zhang, An investigation of V_2O_5/polypyrrole composite cathode materials for lithium-ion batteries synthesized by sol–gel, Mater. Sci. Eng., B **177,** 929 (2012).

[33] M. L. Qian, Y. J. Zhao, and Q. Cheng, Contrast mechanism of phase image in tapping mode of scanning probe acoustic microscope, Acta Acustica **35,** 289 (2010).

[34] Y. J. Zhao, Q. Cheng, and M. L. Qian, Frequency response of the sample vibration mode in scanning probe acoustic microscope, Chin. Phys. Lett. **27,** 056201 (2010).

[35] B. Zhang, Q. Cheng, M. Chen, W. Yao, M. Qian, and B. Hu, Imaging and analyzing the elasticity of vascular smooth muscle cells by atomic force acoustic microscope, Ultrasound Med. Biol. **38,** 1383 (2012).

[36] Y. Liu, D. Guan, G. Gao, X. Liang, W. Sun, K. Zhang, W. Bi, and G. Wu, Enhanced electrochemical performance

[37] A. Watanabe, Highly conductive oxides, $CeVO_4$, $Ce_{1-x}M_x$ $VO_{4-0.5x}$ (M = Ca, Sr, Pb) and $Ce_{1-y}Bi_yVO_4$, with zircon-type structure prepared by solid-state reaction in air, J. Solid State Chem. **153,** 174 (2000).

[38] V. M. Mohan, B. Hu, W. Qiu, and W. Chen, Synthesis, structural, and electrochemical performance of V_2O_5 nanotubes as cathode material for lithium battery, J. Appl. Electrochem. **39,** 2001 (2009).

[39] C. V. S. Reddy, S. Mho, R. R. Kalluru, and Q. L. Williams, Hydrothermal synthesis of hydrated vanadium oxide nanobelts using poly (ethylene oxide) as a template, J. Power Sources **179,** 854 (2008).

[40] R. Das, S. Giri, A. M. Muliwa, and A. Maity, Highperformance Hg (II) removal using thiol-functionalized polypyrrole (PPy/MAA) composite and effective catalytic activity of Hg (II)-adsorbed waste material, ACS Sustainable Chem. Eng. **5,** 7524 (2017).

[41] W. Bi, J. Huang, M. Wang, E. P. Jahrman, G. T. Seidler, J. Wang, Y. Wu, G. Gao, G. Wu, and G. Cao, V_2O_5–conductive polymer nanocables with built-in local electric field derived from interfacial oxygen vacancies for high energy density supercapacitors, J. Mater. Chem. A **7,** 17966 (2019).

[42] S. Peshoria and A. K. Narula, In-situ preparation and properties of gold nanoparticles embedded polypyrrole composite, Colloids Surf., A **555,** 217 (2018).

[43] S. A. Naayi, A. I. Hassan, and E. T. Salim, FTIR and xray diffraction analysis of Al_2O_3 nanostructured thin film prepared at low temperature using spray pyrolysis method, Int. J. Nanoelectron. Mater. **11,** 1 (2018).

[44] K. S. Khashan, G. M. Sulaiman, F. A. Abdulameer, S. Albukhaty, M. A. Ibrahem, T. Al-Muhimeed, and A. A. AlObaid, Antibacterial activity of TiO_2 nanoparticles prepared by one-step laser ablation in liquid, Appl. Sci. **11,** 4623 (2021).

[45] Y. Liu, L. Wang, W. Jin, C. Zhang, M. Zhou, and W. Chen, Synthesis and photocatalytic property of $TiO_2@V_2O_5$ coreshell hollow porous microspheres towards gaseous benzene, J. Alloys Compd. **690,** 604 (2017).

[46] M. Šetka, R. Calavia, L. Vojkůvka, E. Llobet, J. Drbohlavová, and S. Vallejos, Raman and XPS studies of ammonia sensitive polypyrrole nanorods and nanoparticles, Sci. Rep. **9,** 8465 (2019).

[47] Y. Li and L. Zhang, Improving Li ion storage capability of V_2O_5 Electrode by using aminoalkyldisiloxane electrolyte additive, ChemistrySelect **7,** e202202877 (2022).

[48] Y. Wang, J. Zhang, and Y. Zhao, Strength weakening by nanocrystals in ceramic materials, Nano Lett. **7,** 3196 (2007).

[49] N. Muralidharan, C. N. Brock, A. P. Cohn, D. Schauben, R. E. Carter, L. Oakes, D. G. Walker, and C. L. Pint, Tunable mechanochemistry of lithium battery electrodes, ACS Nano **11,** 6243 (2017).

[50] Z. Huang, C. Pan, P. Huang, P. Si, W. Wu, C. Xu, J. Zhou, and X. Li, Effects of ZnO nanoparticles on the microstructure, mechanical properties and wettability of polypyrrole–polydopamine nanocomposites coated on W substrate, Mater. Today Commun. **28,** 102620 (2021).

[51] A. Q. Pan, H. B. Wu, L. Zhang, and X. W. Lou, Uniform V_2O_5 nanosheet-assembled hollow microflowers with excellent lithium storage properties, Energy Environ. Sci. **6**, 1476 (2013).

[52] Y. Bo, X. Li, Z. Bai, M. Li, D. Lei, D. Xiong, and D. Li, Superior lithium storage performance of hierarchical porous vanadium pentoxide nanofibers for lithium ion battery cathodes, J. Alloys Compd. **634**, 50 (2015).

[53] S. P. Timoshenko and J. N. Goodier, *Theory of Elasticity*, 3rd ed. (McGraw-Hill, NewYork, 1970).

[54] W. L. Wang, S. Lee, and J. R. Chen, Effect of chemical stress on diffusion in a hollow cylinder, J. Appl. Phys. **91**, 9584 (2002).